PRECISION AND ACCURACY OF TRIDIMENSIONAL LOCALIZATION IN STATSCAN DIGITAL MEDICAL RADIOLOGY:

BY

JACINTA SYOKAU KIMUYU

UNIVERSITY OF CAPE TOWN

SUPERVISED BY

PROF. HEINZ RÜTHER
Professor of Geomatics Engineering

JUNE 2006

Thesis submitted to the University of Cape Town in fulfillment for the award of Master of Science in Engineering degree.

Declaration

I, Jacinta Syokau Kimuyu, confirm that the content of this thesis is my original work. Where other peoples' work has been cited, it has been appropriately acknowledged.

Disclaimer

The information found in this research is not intended to be used as a substitute for existing medical diagnosis methods by any practicing Medical Doctor. However, if the medical fraternity considers the approach to be of considerable contribution, I have no objection on the method being used in clinical applications.

Acknowledgements

The author would like to express sincere gratitude to the following individuals and organizations:-

Prof. Heinz Rüther, my supervisor, for invaluable time committed to structuring this work, constructive critique, provision of required software/equipment and incessant encouragement.

Deutscher Akademischer Austausch Diennst/DAAD e.V. German Academic Exchange Service, for Scholarship offer.

Lodox (Pty) Ltd. for allowing access to the Statscan Digital Radiology System and research facilities.

Greg Flash, Lodox (Pty) Ltd. research Manager, for assisting with data acquisition on the Statscan system and providing required research information.

Prof. Kit Vaughan, Head of Biomedical Engineering Dept. (UCT); for facilitating learning of course work at the Faculty of Health Sciences.

Dr. Tania Douglas, Dr. Ernesta Meintjes and Dr. Lester John, Biomedical Engineering academic staff and my lecturers in Medical Imaging.

Jenny Whittal (Ms), Geomatics academic staff (UCT), for aptitude to listen and offer encouraging research advice.

Sandra Davids (Mrs), Geomatics support staff (UCT), for amity and administrative assistance.

Dirk Matthee (Mr), Peter Chifamba (Mr), Sydney Smith (Mr), Geomatics support staff (UCT), for technical assistance.

Prof. Francis W.O. Aduol, Principal, College of Architecture and Engineering; and the entire University of Nairobi, Kenya, for invaluable support.

Lastly and not least, I am beholden to my family, and more highly to Sammy and Moses, the boys of my youth, for their fortitude during my absence.

Abstract

The emergence of computerized medical imaging in early 1970s, which merged with digital technology in the 1980s, was celebrated as a major breakthrough in three-dimensional (3D) medicine. However, a recent South African innovation, the high speed scanning Lodox Statscan Critical Digital Radiology modality, has posed challenges in X-ray photogrammetry. This is due to the system's imaging geometry. This research investigates the applicability of Direct Linear Transformation (DLT) method in Lodox Statscan 3D point localization. Static models designed from metal frames bearing targets of different contrast have been imaged on the Statscan system to generate experimental data. These models were used to eliminate distortions that arise from involuntary human body movements. A control frame for the 3D models has been generated at an accuracy of $\pm 0.5mm$. Point positioning accuracy has been computed by comparing the acquired Statscan 3D point positions to the established control.

Two different reference frames were used, showing that point positions could be established with RMS values in the *mm* range in the middle axis of the Statscan X-ray patient platform. This range of acceptable *mm* accuracies extends about 15 to 20 cm sideways towards the edge of the table and to about 20 cm above the table surface. Beyond this range, accuracy deteriorated significantly. The experiments further showed that the inclusion of control points close to the table edges and more than 20 cm above the table resulted in lower accuracies for the L - parameters of the DLT solution than those derived from points close to the center axis only. As the accuracy of the L - parameters propagates into accuracy of the final coordinates of newly determined points, it becomes essential to restrict the space of the control points to the above described limits.

If one adopts the usual approach of surrounding the object by known control points, then the limited space with an acceptable accuracy potential for the L - terms would not be large enough to enclose an adult human body surrounded by suitably positioned control points. This shortcoming can be overcome by making use of two further observations made in the course of this investigation. These observations were firstly, that the best image orientation angles are 0^0 and 40^0 to 60^0, and secondly that no significant improvement could be achieved when using more than two images. The possible observation method deduced from this is as follows:-

1. A frame with well distributed control points with accurate 3D coordinates and of approximately the size of a human body is placed on the X-ray table and imaged with the X-ray beam in the 0 degree position. This makes it possible to determine L parameters for this ray orientation.
2. The frame is removed; the patient is positioned in the control space; and an X-ray image of the patient is taken.
3. The X-ray source is rotated to a new position between 40^0 and 60^0 and a second image of the patient is acquired.
4. The patient is removed and replaced by the frame. A final image of the frame is now acquired.

Steps 1 and 4 serve to determine the L-parameters for the two X-ray source positions, while steps 2 and 3 provide the image coordinates of the required object points on or inside the patient's body. This approach can only then result in accurate point positions, if the patient remains motionless for the duration of steps 2 and 3. An alternative to this observation design would be simultaneous imaging from two X-ray sources, one with 0^0 orientations and the other with an orientation between 40^0 and 60^0.

A further restriction in the use of the scanner as a 3D positioning device results from the need for well defined point. This means that positions on soft tissues cannot be determined unless the required points are clearly defined in the scan images. Positions and dimensions of bones and foreign objects inside the human body are easier to establish.

Table of contents

List of Figures

Page

List of Tables

Page

CHAPTER ONE

1.0 INTRODUCTION

Statscan Critical Digital Radiology (DR) is a flexible format digital imaging system, which is based on enhanced linear slit/slot scanning technology that uses a linearly moving focal spot origin. High quality digital outputs of radiographic images are acquired from the system. Stascan digital technology was developed in 2003 by Lodox (Pty) Ltd., and can be traced back to the South African mining industry. The forerunner of Stascan was a digital X-ray security system (Scannex) owned by De Beer' diamond mines. Mine workers were scanned randomly as they exited the mines to prevent in-the cavities gems theft. Scanning was in standing mode (see figure 1-1(a)), where workers had to pass through the X-ray system and were exposed to radiation. A significant design modification of the security system to be used in medical radiology is the introduction of a patient platform as shown in figure 1-1 (b).

(a) 

(b) 

Figure 1-1 De Beers Scannex (a) and Lodox Statscan System (b)[1]

[1] Diagrams' source: http://www.lodox.com

The Statscan system has continued to gain popularity worldwide since invention. Today, this medical device has become a life saving device for critically injured patients around the world. Apart from the systems locally installed in South African hospitals, the scanner has already been installed in 10 US hospitals, and has received full approval from the US Food and Drug Administration. Denis Wang, the medical director of trauma division in Washington Hospital Center, has reported the efficiency of Statscan in quick and accurate diagnosis. This technology has facilitated rapid patient throughput in trauma care and treatment 'see http://www.lodox.com/'. As reported by the Lodox Product manager, Rodney Sandwith, in the South African Innovation article (2005), the company has recently being contracted to supply the Sudanese government in Africa with four Statscans worth US $ 1.2-million (eg. South African Innovations (2005);http://www.southafrica.info/ess_info/sa_glance/scitech/statscan.htm).

1.1 BACKGROUND OF DIGITAL MEDICAL RADIOLOGY

The advent of computer technology and emergence of diverse digital medical imaging modalities has combined to revolutionize imaging techniques in diagnostic medicine. The 1895 accidental discovery of X-rays by Wilhelm Conrad Röntgen paved the way for radiology as a new medical diagnosis technique in the first decade of 1900's. Digital imaging modalities were implemented in the 1970's with the first clinical use and acceptance of Computed Tomography (CT) scanner 'eg. http://www.imaginis.com/faq/history.asp?mode=1'. The CT scanner, which was invented by Godfrey Hounsfield, was originally referred to as Computerized Axial Tomography (CAT) scanner. As reported in Philips medical systems' Tomoscan CX/Q[2] operators' manual, the non-homogenous nature of anatomical structures is attributed to a CT

[2] The operators' manual was used by the author of this research in undergraduate thesis (unpublished)

number on the Hounsfield scale to represent the density of body tissues. The gray scale ranges from 0 (black) that represents high X-ray penetration in fatty tissue to 255 (white) associated with low radiation penetration in bone tissue.

Contrast enhanced angiography of blood vessels and procedural catheterization are some of the medical procedures that have benefited from the adaptation of digital radiology technology. However, this technology still remains as works-in-progress in most developing countries, where X-ray systems from the pioneering age remain indispensable in medical radiology. Over the years, medical experts dispatched from developed countries to respond to disasters occurring in developing countries have brought with them high-tech medical equipment 'e.g http://www.neuroscicncccenter.com/NCoW/x-ray.html'.

Important to note are the significant prognostic benefits and advantages of digital technology to all X-ray systems. Some of the most remarkable attributes of digital radiology are:

- digital image processing techniques can be applied to enhance the generated X-ray images;
- reduced radiation dose and High Detection Quantum Efficiency (DQE) can be achieved through digital X-ray technology;
- digital images from digital radiology and those digitized from conventional images can be sent by advanced electronic communication thus enabling medical consultation with distant specialists in the field of e-medicine; and also provide data sharing through hospitals' computer network to facilitate timely diagnosis and simultaneous procedural medical planning;

- digital image archiving of digital radiology images like digitized conventional images on compact optical disks/digital tape drives or similar data carriers can save on storage space and reduce the manpower needed for management of routine traditional X-ray film libraries;
- future reference of the clinical diagnostic radiographs can be done by image retrieval from the documented digital archives of images obtained from digital radiology and also those digitized from conventional images.

Despite the listed advantages of digital X-ray images, their usefulness is still limited in representation of reality in human anatomy, just as in conventional X-ray diagnosis. Mainly, the two-dimensional X-ray image generated for medical diagnosis has no volumetric capability and therefore:

- the two-dimensional (2D) images obtained in X-rays are a complex superposition of all the three-dimensional (3D) body structures and thus difficult in interpretation;
- there is no perception of depth (i.e. third dimension is lost);
- the image size of an object is dependent on its distance from the X-ray source resulting in different scale factor for one image;
- the contrast of the image suffers from limited dynamic range of the attenuation coefficients that exist in the human body.

'see e.g http://www.nuclear.kth.se' .

1.2 RESEARCH OBJECTIVE

The aim of this research is to generate a method for reconstructing the third-dimension from two-dimensional (2D) X-ray images acquired using Stascan Digital Radiology system. Precision and accuracy in three-dimensional (3D) localization of points of interest on static models made of 3D metal frames will be investigated.

1.3 RESEARCH PROBLEM JUSTIFICATION STATEMENT

Statscan digital X-ray output is usually in the form of two-dimensional images. The system can produce a full body radiograph with extremely low X-ray dosage as compared to Computed Tomography (CT) systems. However, without the capability of 3D imaging, the Statscan cannot be used as an alternative to CT systems in applications that require 3D diagnosis.

A technique for localization of points of interest in three-dimensional space will be investigated to establish if Statscan can appropriately be used in clinical applications that do not require the 3D volume. The scanning speed and quality radiography of the Statscan has greatly revolutionized digital radiology, but the 2D output still remains an inferior representation of human anatomy. As stated above, the Statscan imaging technology is cost – effective and exposes the patient to less X-ray dosage than other methods like CT-scanning. Thus an extension of the Statscan output to 3D-data will be highly desirable.

1.4 METHODOLOGY AND PROCEDURES APPLIED

The first step was the design of two 3D metal frames of different sizes with reflective targets. The targets were visible on photographed images. Since the same 3D metal frames were scanned using the Statscan system, the targets were made of material of a different density from the joining metal bars. The use of static metal frames on the Statscan machine was aimed at testing the performance of the system in terms of accuracy in 3D reconstruction using images taken from different orientations. A static frame model was used for the investigation of the 3D potential of the scanner instead of imaging a human body to eliminate the additional distortions caused by involuntary body movements. The measurement of soft tissue and bones was not done due to the difficulty to find distinct marks on the internal structures of the human body. This aspect will have to be explored in further research. The two different metal frames that were used are shown in figure 1-2.

Figure 1-2 Metal frame models of different sizes.

Each metal frame contained two sets of points, the control points and the test points to be reconstructed from the Statscan images. Visible

targets on the frames were chosen as control, and different combinations and numbers of control points were explored to determine the optimal control configuration; while the rest of the points formed the test points. Digital photogrammetry method was used to provide the space positions for both the control points and the test points. Initially, the space positions for the test points were taken as unknown, and to be determined from Statscan images. The results obtained from 3D reconstruction using Statscan images were compared to the space positions of test points to establish point reconstruction accuracy.

In order to provide an independent check for the control and test data, a precise theodolite positioning method was used to acquire a separate three-dimensional data set. The two data sets were compared by means of a three-dimensional similarity transformation of the digital photogrammetric coordinates into the positions derived by theodolite measurements. The rigid body transformation uses a mathematical model that preserves the relative space positions of the points being transformed. Prior to the transformation of the coordinates from one system to the other, the object and target systems should both be in either right-hand or left-hand coordinate system. After computation and confirmation of agreement between the two methods, one set of space control will be used in X-ray 3D reconstruction.

X-ray photogrammetry is based on central projection. In spite of the finite size of the focal spot, the mathematical model for image generation is the central projection (Veress and Karara, 1989). X-ray photogrammetry is a modification of the usual photogrammetric space resection and intersection procedure based on the collinearity equation, which was modified to accommodate X-ray photogrammetry (Veress et al., 1979). Although the X-ray modality being used in this research differs from the conventional X-ray system, thus Direct Linear Transformation (DLT) method will be used.

The standard Direct Linear Transformation (DLT) which was originally proposed by Abdel-Aziz and Karara (1971) was used to reconstruct the 3D coordinates of targets on the metal frame from Statscan images. The same method has been used by staff and research students from Biomedical Engineering at the University of Cape Town in an attempt towards 3D reconstruction. The transformation from the 2D Statscan image coordinates to 3D object space using the DLT model required an iterative least squares adjustment. DLT relates the image coordinates (x_i, y_i) of a point to its corresponding three-dimensional object coordinates (X_i, Y_i, Z_i) through 11 transformation parameters(L_{ij}). The transformation parameters will be solved iteratively by use of the known control point positions on the 3D metal frame.

The internal accuracy or precision of the DLT parameters for each image was determined from the variance-covariance matrix of the least squares adjustment of the images acquired from different orientations. The accuracy of the 3D localization was computed by comparing the 3D coordinates obtained using images from the Statscan system with those from digital photogrammetry. By transforming the set of coordinates into the coordinates derived by the digital photogrammetry method, the magnitude of the root mean square error in computed 3D space coordinates was established. The trend in change of positioning accuracy with different image combinations, taken from different orientation angle, if any such trend occurred, was investigated. The flow chart in figure 1-3 outlines the method procedures.

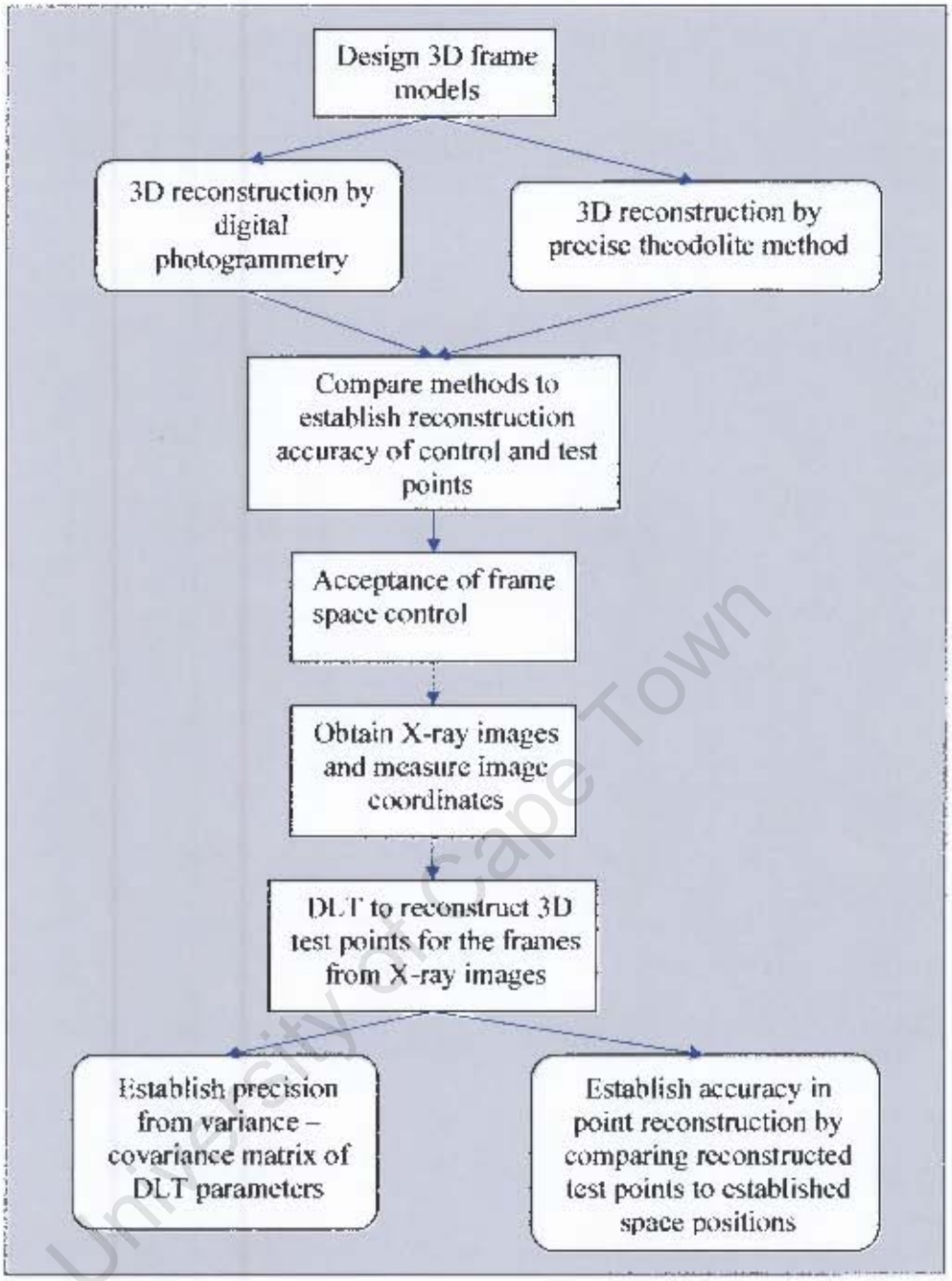

Figure 1-3 Steps to be followed in research.

1.5 EQUIPMENT AND INSTRUMENTATION

In order to accomplish the outlined tasks in this research and achieve the set objective, the following equipment and instruments were required:-

Item No.	Description	Purpose
1	3D metal frame models of different sizes (two)	Provide control and test points to be reconstructed in 3D space.
2	Nikon *D100* digital camera with 28 mm lens	Provide digital photographs of the metal frames models.
3	Retro-reflective targets (more than 50 in number)	Provide camera calibration test field.
4	Total Station, three tripods, tribrach and two targets	Provide data for precise theodolite positioning.
5	Least Squares adjustment programme (existing parametric case)	Adjustment of the provisional $x, y-$coordinates to compute the final $z-$coordinates in theodolite positioning.
6	Digital X-ray system (Lodox Statscan system)	Provide 2D digital radiographs of the metal frames.
7	*Australis* photogrammetric software	For camera calibration and 3D reconstruction by digital photogrammetry method.
8	*Matlab* Mathworks software	Matrix computations.

Table 1-1 Required equipment and instruments.

CHAPTER

TWO

2.0 THREE DIMENSIONAL MEDICAL IMAGING

2.1 DIGITAL PHOTOGRAMMETRY IN MEDICINE

The basis of modern digital photogrammetric metrology is the CCD cameras, whose use has permitted the acquisition of images of very large dynamics. The term 'photogrammetric metrology' covers the whole range of metrology activities that exploit photogrammetric processes based on image acquisition and image processing, that historically hardly ever took place in real time (Kasser and Egels, 2002). The appearance of digital imagery has been the origin of a significant change in this technical domain and real time measurements can be obtained. Digital photogrammetry is the technique of measuring 3D objects from imagery acquired by video/CCD cameras or radiation sensors such as scanners. In other words, digital photogrammetry is the branch of photogrammetric technology, where the illumination in the image plane of the camera is not recorded photographically, but by electronic means. Karara (1989) defines digital photogrammetry as a sequential process in which an image is acquired digitally and then processing is executed in computers. The process involves the use of picture elements (pixels) and image processing techniques to arrive at geometric information. Computerized techniques have been used that simulate human vision and pattern recognition/image understanding.

A pixel, the portmanteau of 'picture elements', is the basic component in digital image representation. A digital image is a regular array of pixels, or picture elements, and it can be described in terms of

geometry and radiometry (Mikhail et al., 2001). Digital images appear like a smooth continues image on a computer screen, or on a printed hard copy. Photogrammetric accuracy increases with decrease in pixel size. The digital data acquired can be modified through image processing and preserved for later retrieval when required. The use of high-resolution digital cameras in conjunction with retro-reflective targets has enabled highly-automated, high-precision close-range photogrammetric measurements. The term close-range photogrammetry has been used for photogrammetric procedures that are performed using images taken when the object-to-camera distance is generally less than 100m (Marzan and Karara (1976)).

There are two types of sensors used to record information in non-topographic photogrammetry. The active sensors are those that generate generate their own energy, transmit it to the object and record the energy returned to the object. The passive sensors on the other hand are those that record energy reflected off the object with an external source of energy to the sensor. Photogrammetric metrology has been useful in the following domains:-

- When the measure must be acquired in a very short time on numerous points;
- When measures are to be performed without possible or desirable contact (very hot objects or measures contaminated objects);
- When measures can be exploited a long time after the acquisition of the images of a scene.

2.2 HISTORY IN THE SEARCH FOR THE MEDICAL THIRD DIMENSION

In the year 2002, Dr R. Van Tiggelen[3] documented the history on the search for the third dimension, from radiostereoscopy to three-dimensional imaging. In the article, a radiographic image has been defined as the sum of the shadows of all the objects located between the radiation tube and the photographic media. Such an image is therefore, in Tiggelen's words, 'the bidimensional projection of the tridimensional volume'. The recorded image shadows are superimposed as the levels at which they are located and cannot be discretely determined. The image shadows need to be dissociated for any meaningful interpretation to be made from X-ray images.

The procedures and principles of binocular vision have been applied to radiology by obtaining two images with no patient movement. The X-ray tube in this procedure is moved in a well determined course. Tiggelen further reports that the first application in radiology is in the Electrical Engineer article by E. Thomson (1896, March 11), entitled 'Stereoscopic Roentgen pictures'. Within the same year (1896), G. Contremoulins practiced stereography for vascular studies on corpses. The subsequent numerous trials entailing measurements by means of stereography proved the feasibility to use the stereoscopic parallax to localize and determine the depth of a metal foreign object in a patient's body. Although stereoscopy was found to be a useful method, it was still not a major breakthrough; while stereography continued to be used by most radiologists. Stereography was soon overtaken by tomography, but the technique of stereography survived longer in the United States of America (USA), until the discovery of slice tomography in the mid 1930s by J. Kieffer. Stereography remained in practice most

[3] Belgium Museum of Radiology curator, Queen Astrid Military Hospital, Bruynstreet 2, B-1120 Brussels, Belgium.

particularly in cardiovascular radiology until the end of the 20th Century.

In the period from 1900 onwards, the growing interest in the technique stimulated both the concept and the manufacturing of equipment for stereoscopic viewing throughout the world. In 1928, B.G. Ziedse Des Plantes developed slice tomography and also stereoscopic techniques. He finalized a prototype of Tomography in August, 1931, which he called planigraphy. Plantes published the first clinical results obtained on the human skull and spine in the same year. J. Kieffer also investigated the principle of planigraphy in 1928, with an aim to produce radiographic images to visualize his own pulmonary lesions. Kieffer's method was patented in 1934 and commercialized in 1938 by the American 'Keleket X-ray' company.

Another independent development was by A. Vallebona who obtained his first radio-tomographic image in 1930. He described two techniques whereby in the first one, the subject would remain immobile as the system (X-ray tube plate) pivoted around an axis situated at the level of the slices. In the second technique, the system (X-ray tube and film) remained immobile while the patient rotated around an axis situated in the level of obtaining the images. In 1934, during the 4th Congress of Radiology in Zurich, H. Chaoul and G. Grossmann presented the results obtained with a new tomography technique, which was commercialized in 1935 by the Berlin Company, Sanitan.

Tiggelen continues to report that the real revolution for three-dimensional medical imaging coincided with the use of digital computers for image reconstruction, together with the commercial launch of X-ray Tomography (CT). Due to the frustrations from the limitation in X-ray CT, in 1972, Sir Godfrey Hounsfied, an engineer in the British firm EMI (Electro-Musical-Instruments), devised a method

for creating an image in great detail of narrow cross-sections of a portion of the human body. Up to date, Hounsfied's technique is used in X-ray radiology and three-dimensional visualization. The first Magnetic Resonance Imaging (MRI) scanner was introduced to the world during the April 1980 annual meeting of the American Roentgen Ray Society. Later in the same year, the MRI Scanner was introduced again at the annual meeting of the Radiological Society of North America (RSNA).

We can therefore state that over the seventy years following the accidental discovery of X-rays, several attempts have been made to develop imaging techniques for three-dimensional imaging. The medical imaging techniques developed include Computed Tomography (CT) that can produce three-dimensional slices of the human body. The acquired slices are assembled by Multi-planar Reformatting (MPR) techniques and computer graphics for three-dimensional visualization. The MRI technique has proved to be quite useful in detecting soft tissue abnormalities and injuries. However, digital X-ray technique, which is basically conventional X-ray, still produces two-dimensional images of superimposed anatomical features, thus the need for development of three-dimensional reconstruction methods.

2.3 OVERVIEW OF DIGITAL X-RAY TECHNOLOGY

Digital X-ray techniques are a modification of the conventional X-ray photogrammetry that has been extensively used in the field of medicine over decades. On 8th Nov, 1895, Wilhelm Conrad Röntgen discovered an image cast from his cathode ray generator, projected beyond the possible range of the cathode rays, which is presently known as an X-ray beam. Further investigation showed that the rays were generated at the point of contact of the cathode ray beam on the interior of the vacuum tube. The rays were not deflected by magnetic fields, and they penetrated many kinds of matter. Shortly after his discovery, Röntgen took an X-ray photograph of his wife's hand which clearly revealed her wedding ring and her bones. The photograph electrified the general public and aroused great scientific interest in the new form of radiation. Röntgen named the new form of radiation he discovered X-radiation (X standing for "Unknown"), 'e.g http://www.inventors.about.com/library/inventors/blxray.htm '. The first X-ray picture taken by Röntgen is shown in figure 2-1.

Figure 2-1 X-ray picture of Mrs. Röntgen's hand (the first X-ray picture ever taken)[4]

[4] Diagram source: http://inventors.about.com

The images produced by X-rays are due to the different absorption rates of the different body tissues. Image resolution in X-ray technology has greatly advanced since invention. Calcium in bones has the highest absorption for the X-rays, so bones look white on a radiograph, a film recording of the X-ray image. Body fat and other soft tissues absorb less, and hence they appear gray on the radiograph. Air absorbs the least, so lungs look black on a radiograph. In digital X-ray imaging, objects are irradiated by photons from an electronic source and the transmitted photons are registered electronically on CCD detectors. In principle, X-ray attenuation in tissue is proportional to electron density, thus the X-ray intensity that traverses a region of lower electron density (muscle) will be greater than that which has traversed a region of higher density (bone). This means that the gray level of the image is proportional to the attenuation of the tissue in the gray path (0 – 255) range ' e.g http://www.nuclear.kth.se '.

Digital (or computerized) imaging techniques became part of X-ray technology in the 1980s when analog to digital (A/D) converters and computers were adapted to conventional fluoroscopic image intensifier/TV systems. The manufacturers and researchers around the world have taken digital X-ray detectors from the lab and into clinical trials. This is indeed a significant breakthrough in X-ray imaging and diagnostic radiology has been greatly revolutionized. The radiologist views the results of fluoroscopic or X-ray examination in real time using a digital X-ray system (see figure 2-2). With digital technology, X-ray signals are converted into digital images at the detector itself, with the images digitized into a matrix of pixels with each pixel being coded digitally.

Figure 2-2 Digital X-ray Imaging System[5]

2.3.1 Lodox Statscan™ Digital Radiology (DR)

The Statscan system can provide scans of both bone and soft tissue that are of high diagnostic quality for a wide range of traumatic injuries. This system has been used to acquire a full human body scan in at most 13 seconds, critically saving lives in the 'golden hour' of emergencies. As reported in Lodox website, a 25% lower X-ray dose as compared to conventional X-rays renders the scanner a safer choice for doctors, before making a decision to use other high dose and time consuming scanners like the CT-scan. It can as well be used for routine radiology where conventional X-rays have been used over years. The digital scans can be transferred across the hospitals' computer network and further processed without any data loss from image quality degradation. The fact that no X-ray films and cartridges are required has greatly reduced operating costs. Medical experts receive the digital images in near real-time after scanning the patients.

[5] Source: http://www.gehealthcare.com

Figure 2-3 shows sample of high resolution images acquired using Statscan system.

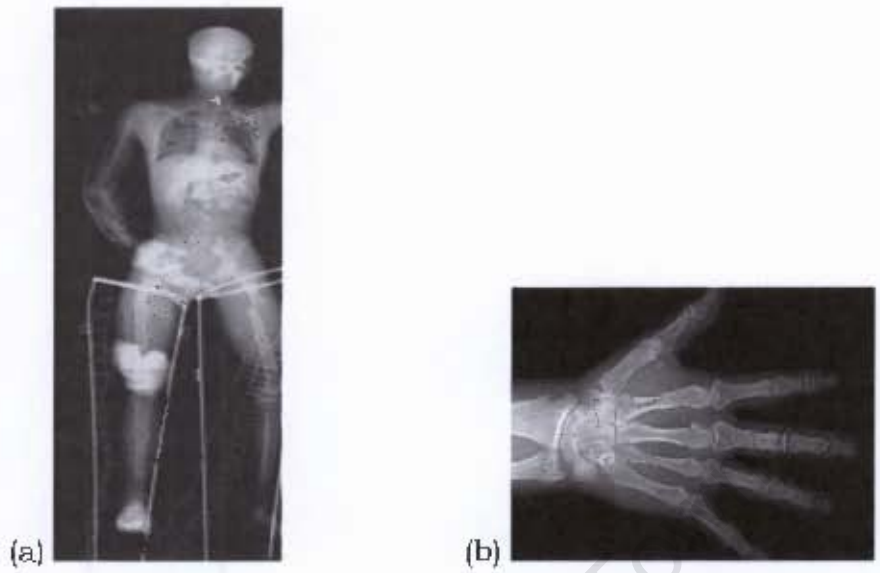

Figure 2-3 Images of multi-fractured full-body of human male (a) and part of a body image (b) taken with Statscan system[6]

Over a period of more than two years, the Statscan technology has attracted the interest of many researchers, mostly clinical experts. A study conducted at the trauma unit at Groote Schuur Hospital at the University of Cape Town in South Africa (Lodox website), has reported that the system has offered some significant improvement in patient handling, with time required to complete diagnostic examination reduced from 48 to 5 minutes. More over, the study showed that the radiation exposure to both medical staff and patients was lower as compared to conventional X-ray devices. Stascan has an open design that can allow continuous medical attendance to critically injured patients during scanning. This versatility has placed the scanner at an edge over many other medical imaging technologies.

[6] Diagram source: http://www.lodox.com

2.4 RELEVANT WORK DONE ON THE STASCAN THREE-DIMENSIONAL POINT LOCALIZATION

Three-dimensional reconstruction of points by means of Lodox Statscan scanner has been reported by researchers in digital medical imaging. This is outlined in a paper submitted by Tania Douglas, et al; on the 26th June 2003 and published in the Medical & Biological Engineering & Computing 2004, vol.42. As stated in the article, "the aim in conducting the study was first to determine the optimum configuration for performing stereo-photogrammetry on images produced by Statscan, in terms of the separation angle between stereo images and the number and configuration of control points in the calibration instrument. Secondly, the study was aimed to determine the reconstruction errors of the method to establish a set of clinical applications for which the method would be suitable."

The method used in three-dimensional localization of points in Douglas' study was adopted from an earlier study by Van Geems et al., (1995) – A two-dimensional projective transformation for the calculation of three-dimensional CT coordinates of image points from CT scan projective radiographs (SPRs). Douglas reports that this method was initially applied to anterior-posterior and lateral SPR pairs, but was later shown to be suitable for oblique views. Douglas further states that the method used in 3D localization resembles DLT and uses x-coordinates to obtain X- and Y- coordinates in object space. The term SPR refers to the digital image obtained by linearly translating the patient with respect to the gantry during X-ray exposure while the angle between the X-ray source and the plane of patient movement remains fixed. Dauglas' report was based on the methodology derived by Van Geems, which has been explained in detail.

Van Geems' study was based on Adams' method, (Adams, 1981). Equation 2-1 is the surview equation developed by Van Geems along similar lines as Adams' method.

$$x_i = (h_{k11} - x_i * h_{k21})X_i + (h_{k12} - x_i * h_{k22})Y_i + h_{k13} \qquad (2\text{-}1)$$

where;

- a point i has surview coordinate x_i and slice coordinates X_i and Y_i;
- the five h parameters $(h_{11}, h_{12}, h_{13}, h_{21}, h_{22})$ pertain to surview k.

CT surviews (*AP* and *LAT*) are obtained from the scanned CT slices. The surview equation is used to solve for the 3D slice coordinates using the *AP* and *LAT* surviews. The two dimensional central projections of the *AP* and *LAT* surviews are shown in figure 2-4.

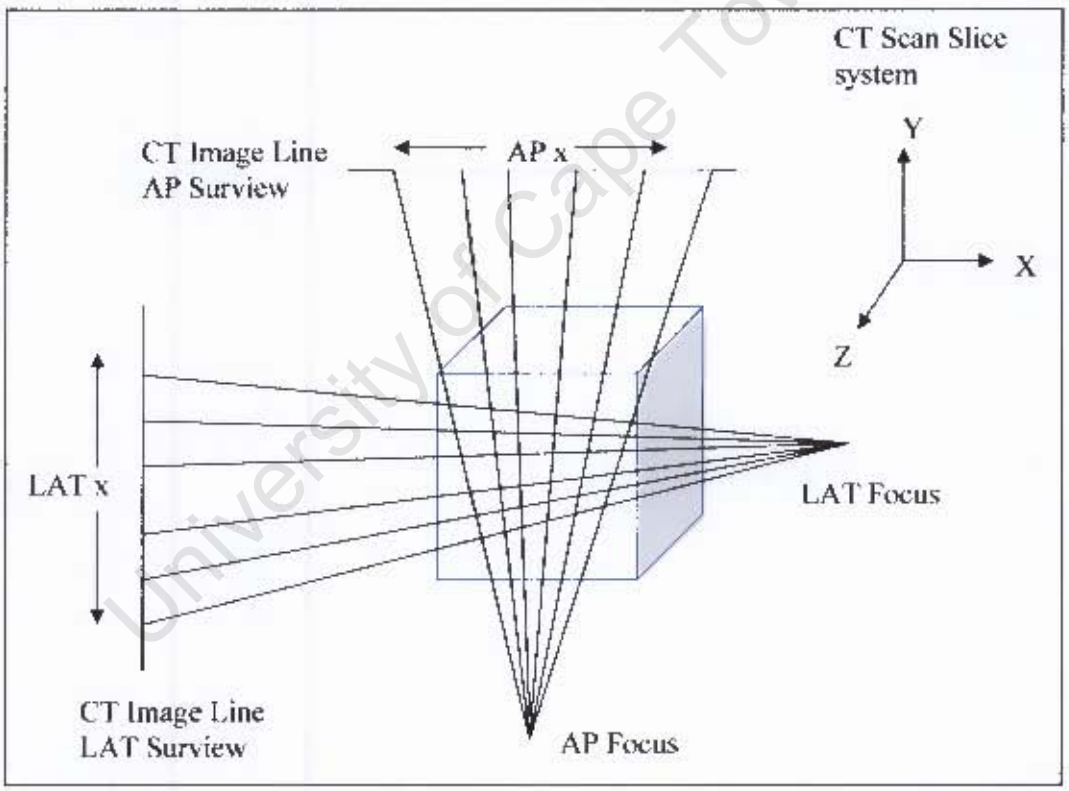

Figure 2-4 The two dimensional central projections of the AP and LAT surviews[7]

[7] Diagram source: Van Geems', pp 44

Van Geems states that two or more surviews of the patient are scanned from different positions on the 360 degree CT gantry circle. The points to be used in determination of 3D coordinates should be visible on the acquired surviews. Before solving for the 3D coordinates of any markers, a minimum of five non-collinear control markers are required to solve for the five *h* parameters for each surview used. In Van Geems' method, a flat glass with markers was used as control. The glass should be set up in the CT scanner in such a way that all control markers appear in one *XY* plane. Van Geems further explains that only one CT slice is required to obtain the 3D slice coordinates for all the control markers. The *AP* and *LAT* surviews of the glass are scanned. For the nine control markers used in the experiment, slice coordinates X_i and Y_i, surview coordinates APx_i and surview coordinate $LATx_i$ were digitized/measured (i denotes the number of control point marker, *i.e* from 1 to 9).

The measured parameters were substituted into the surview equation (equation 2-1). When the *AP* surview parameters were substituted in the equation, only five unknowns remained, that is the *h* parameters. This required the use of five non-collinear markers to obtain a unique solution. Van Geems states that when more than five control markers were used to solve for the *h* parameters of the *AP* surview, there was an over determined case, thus least squares solution was applied to solve for the unknown parameters. Equation 2-1 was rewritten for the *AP* surview as:-

$$x_i = h_{AP11} * X_i + h_{AP12} * Y_i + h_{AP13} - h_{AP21} * x_i * X_i - h_{AP22} * x_i * Y_i \qquad (2\text{-}2)$$

The same process was repeated for the solution of *h* parameters of the *LAT* surview. There were two unknowns X_i and Y_i to be solved for each *AP* and *LAT* slice, requiring a minimum of two equations. Thus each marker should have appeared on both the scanned *AP* and *LAT* surviews. The surview equation was developed by Van Geems from a

linear transformation, equation 2-3, of homogenous coordinates in space, known as a projective transformation when the matrix A is non-singular.

$$\begin{pmatrix} X' \\ Y' \end{pmatrix} = A \begin{pmatrix} X \\ Y \end{pmatrix} \tag{2-3}$$

As reported by Van Geems, in terms of non-homogenous coordinates, equation 2-3 takes the form of equations 2-4, the equations for a two dimensional transformation (Slama, 1980), where a_{ij} is a typical of element A in equation 2-3. The two dimensional projective transformation relates the points on one plane to their corresponding projective positions on another plane.

$$\left.\begin{aligned} X' &= \frac{a_{11}X + a_{12}Y + a_{13}}{a_{31}X + a_{32}Y + a_{33}} \\ Y' &= \frac{a_{21}X + a_{22}Y + a_{23}}{a_{31}X + a_{32}Y + a_{33}} \end{aligned}\right\} \tag{2-4}$$

By dividing the two equations in 2-4, we get:-

$$x = \frac{X'}{Y'} = \frac{a_{11}X + a_{12}Y + a_{12}}{a_{31}X + a_{32}Y + a_{33}} * \frac{a_{31}X + a_{32}Y + a_{33}}{a_{21}X + a_{22}Y + a_{23}} = \frac{a_{11}X + a_{12}Y + a_{13}}{a_{21}X + a_{22}Y + a_{23}} \tag{2-5}$$

The projection between planes is given by equation 2-6, where all the a_{ij} terms are divided by a_{23} and new transformation parameters $h_{ij} = a_{ij} / a_{23}$ are introduced.

$$x = \frac{a_{11}X + a_{12}Y + a_{13}}{a_{21}X + a_{22}Y + a_{23}} = \frac{h_{11}X + h_{12}Y + h_{13}}{h_{21}X + h_{22}Y + 1} \tag{2-6a}$$

$$x = h_{11}X + h_{12}Y + h_{13} - h_{21}xX - h_{22}xY \tag{2-6b}$$

Equation (2-6b) represents the surview equation. Therefore, the *AP* and *LAT* surview equations for determining X_i and Y_i slice coordinates of a marker *i* were expressed as shown in equation 2-7.

$$\left.\begin{aligned} AP_{x_i} &= \frac{h_{AP_{11}}X_i + h_{AP_{12}}Y_i + h_{AP_{13}}}{h_{AP_{21}}X_i + h_{AP_{22}}Y_i + 1} \\ LAT_{x_i} &= \frac{h_{LAT_{11}}X_i + h_{LAT_{12}}Y_i + h_{LAT_{13}}}{h_{LAT_{21}}X_i + h_{LAT_{22}}Y_i + 1} \end{aligned}\right\} \quad (2\text{-}7)$$

CHAPTER

THREE

3.0 DETERMINATION OF SPACE CONTROL FOR THE METAL FRAME MODELS

Two methods will be employed to determine the three-dimensional positions of target points on the big metal frame model. These methods are, as mentioned earlier, digital close-range photogrammetry method and precise theodolite positioning method. The space coordinates for both the control points and test points will be determined. Similar procedure will be repeated for the solution of small metal frame space control. Point positioning accuracy will be established by comparing the results obtained from both methods.

The determined space control data should be reliable for subsequent 3D point localization experiments using Statscan X-ray images. The control points will be chosen from the visible points on all scanned X-ray images that will be used in the 3D reconstruction. Image coordinates of all the visible points will be measured and used together with the control coordinates to solve for the DLT parameters. The solution obtained for the 11 DLT parameters will be used to solve for the 3D coordinates of the test points.

3.1 DIGITAL CLOSE-RANGE PHOTOGRAMMETRY METHOD

3.1.1 Digital imaging using *Nikon D100* CCD Camera

Image acquisition is a fundamental procedure in digital photogrammetry. It is important to plan the project in advance and choose an appropriate camera for the work to be done. However, other factors like camera availability can lead to the selection of a certain type of camera. For this project, *Nikon D100, a "non-metric professional"* camera that was readily available was used. The *Nikon D100* has Charge Coupled Detectors (CCD) and a sensor size of 3008mm pixels in the horizontal direction and 2000mm pixels in the vertical direction.

3.1.2 Camera Calibration procedure for *Nikon D100*

Camera calibration is a pre-requisite procedure in photogrammetric projects, where *amateur* cameras have to be used. This is usually a rigorous task of determining the camera parameters. As reported by Marder (2005), camera self-calibration involves the process of calculating the intrinsic parameters of the camera using only the information available in the images taken by the camera. For a number of images taken by the same camera with fixed internal parameters, correspondence between any three images is sufficient for the recovery of both the internal and external parameters. The cameras' interior orientation elements that should be determined in the calibration process are:-

- the position for the principal point (x_0, y_0);

- the calibration focal length (calibration principal distance) which represents the distance of rear nodal point of the lens to the principal point of the photograph on the image plane (f);
- radial and decentering lens distortions (k_1, k_2, k_3) and (p_1, p_2) respectively (Brown, 1989).

The exterior orientation parameters are also determined. These elements give the angular relationship $(\omega, \varphi, \kappa)$, between image space and the object space coordinate system, and the position of the camera front nodal point during exposure. The camera position in space is X_0, Y_0, Z_0. The camera self-calibrating bundle adjustment technique is highly rigorous, with capability to achieve high accuracy in measurement, and is based on the least squares adjustment model. The stochastic model allows for errors in random observations, while the functional model consists of the collinearity equations. The collinearity equations are based on the assumption that the perspective center, the object and the corresponding image point all lie in a straight line. This condition is not fulfilled in practice due to inaccuracies in the lens/chip assembly and lens distortion. Each pair of observed image coordinates yields two collinearity equations along with the correction for lens distortion (Brown, 1989);

$$x_i - \delta_{x_i} = x_P - c\,\frac{m_{11}(X_i - X_C) + m_{12}(Y_i - Y_C) + m_{13}(Z_i - Z_C)}{m_{31}(X_i - X_C) + m_{32}(Y_i - Y_C) + m_{33}(Z_i - Z_C)} \qquad (3\text{-}1)$$

$$y_i - \delta_{y_i} = y_P - c\,\frac{m_{21}(X_i - X_C) + m_{22}(Y_i - Y_C) + m_{23}(Z_i - Z_C)}{m_{31}(X_i - X_C) + m_{32}(Y_i - Y_C) + m_{33}(Z_i - Z_C)} \qquad (3\text{-}2)$$

where,

(x, y) are the observed image coordinates;

δ_x and δ_y are the lens distortion;

(c) is the camera principal distance;

(x_P, y_P) are the image coordinates of the principal point;

(X_i, Y_i, Z_i) are the object space coordinates;

(X_C, Y_C, Z_C) are the perspective center coordinates in object space;

m_{ij} are the elements of an orthogonal matrix that defines the rotation between the image and the object coordinate system. The elements of the rotation matrix depend on the magnitude of the rotation angles about the axes, the type of the coordinate system (left or right handed), the rotation direction, and the rotation sequence.

3.1.2.1 Camera calibration by *Australis* software

The *Australis* software, (Fraser, 2001) was used for calibration of the Nikon *D100* camera. The software employs self-calibrating bundle adjustment. The object to be measured was imaged from different horizontal and elevation positions and with varying orientations of the optical axes of the camera. The result was a convergent geometry with as many image coordinates for each target as the number of exposures on which the target is visible. The observations of discrete targeted points on the object are used as the data required for determination of the camera calibration parameters (Atkinson, 1996). For a successful self-calibration, the following criteria must be met:-

- At least three images should be taken using the camera to be calibrated, but several cameras can be calibrated at the same time.
- Both the interior geometry of the camera and the point to be measured on the object must remain stable during the measurement process.
- At least one image must have a roll angle that is significantly different from the others.
- A relatively large number of well distributed points should be used.

(see Brown, 1989).

A digital image of a section of the calibration test field used with circular targets on a wall is shown in figure 3-1. The calibration test field is an established control field designed by the Geomatics Division at the University of Cape Town. For this project, 18 images of a test field with 73 reflective targets were used. To initiate the calibration process, the relative orientation method was used with two images taken from parallel camera axes.

Figure 3-1 Calibration test field showing circular target points.

Figure 3-2 shows the labeled target points of an image. The measured image coordinates for each point label have been displayed.

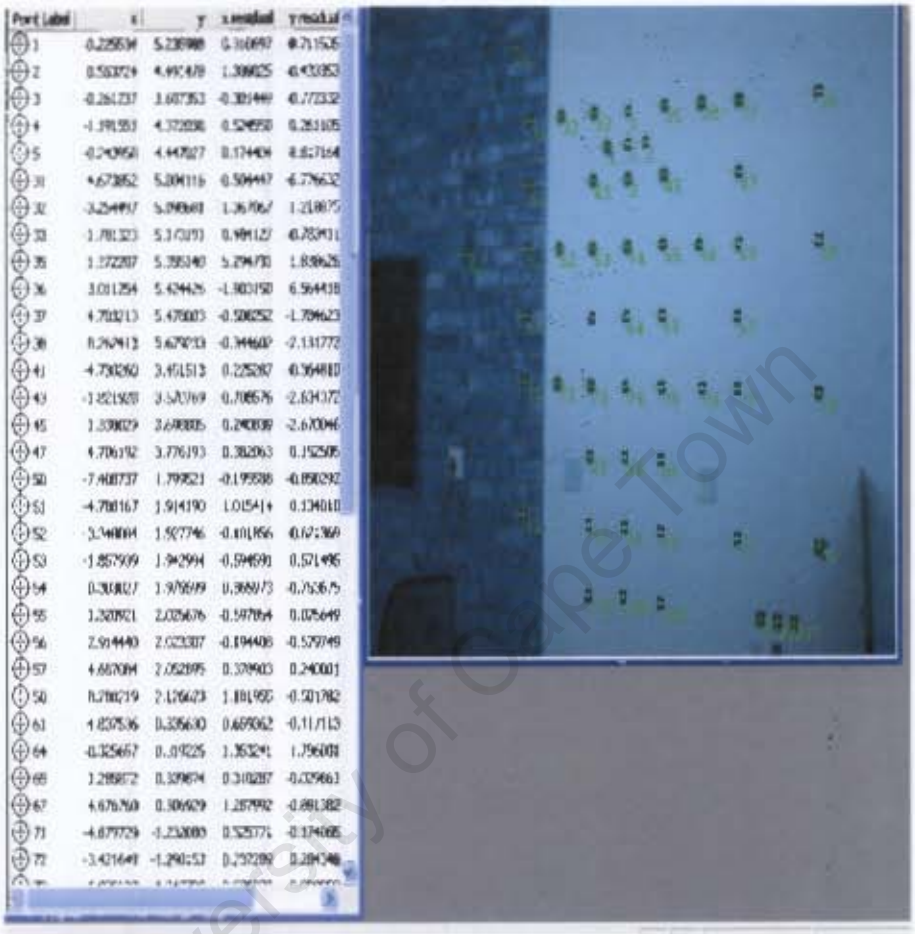

Figure 3-2 Image view with labeled target points and the measured image coordinates.

Figure 3-3 is a display of the *Nikon D100* 28mm lens distortion profiles, as obtained from calibration using *Australis* software.

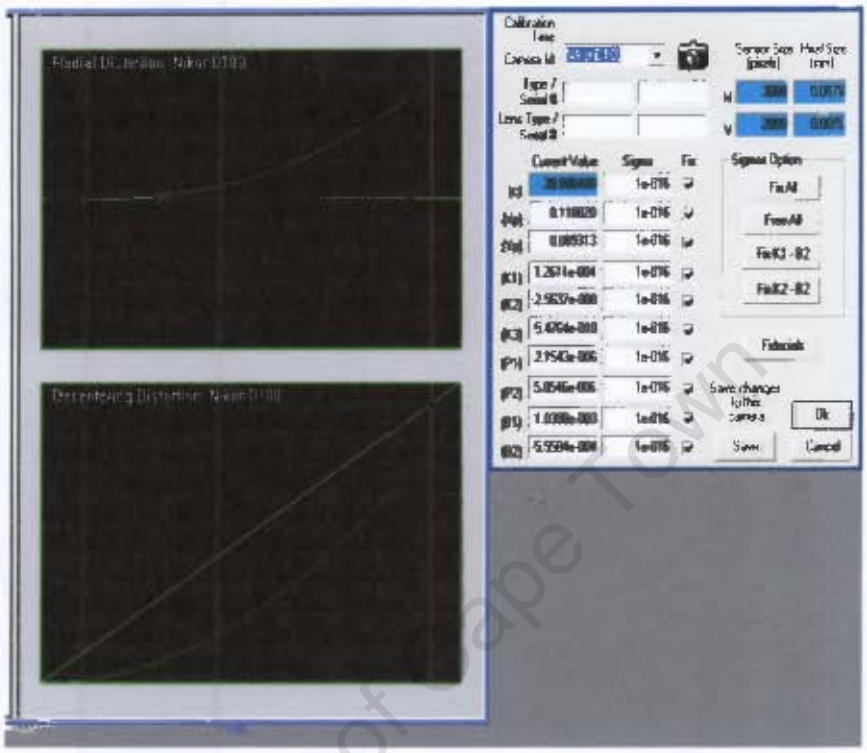

Figure 3-3 Calibration Project view showing Camera calibration database, Radial lens distortion and Decentering distortion plots (the red vertical line limits the CCD format coverage).

An important display tool in *Australis* is the 3D graphics view that displays the measured objects for visualization. This can be used after the points in the images forming the network have been measured. The graphics showing the point cloud generated after the bundle adjustment can then be displayed and the camera stations viewed (see figure 3-4).

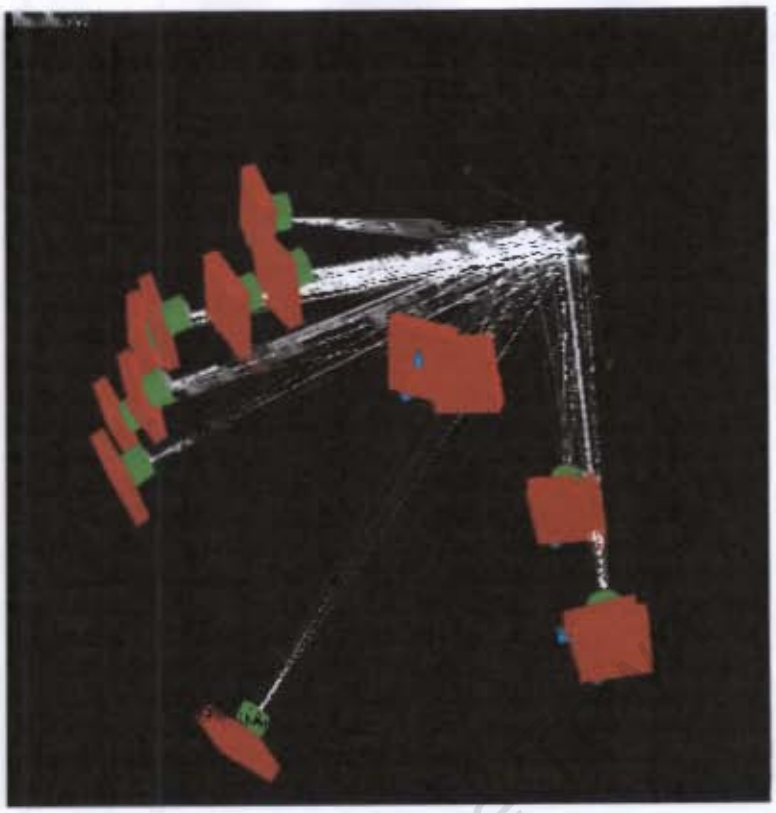

Figure 3-4 Graphics Interface showing intersecting rays to selected points.

3.1.2.2 Computing space coordinates of big metal frame

Further computation of the object space coordinates was done. The calibrated *Nikon D100* 28mm lens camera was used to photograph a 3D metal frame model. A local Cartesian coordinate system was used in this research. Scaling was done using the scalebar tool incorporated in *Australis*. The measured length and width of the metal frame formed the scalebar database. As reported by Fraser (2000), "an important feature of *Australis* is the ability to use scale data, either rigorously in the bundle adjustment as an observed distance of known *a priori* precision, as is needed to support self-calibration in multi-camera networks, or as a means to simply scale the final object space coordinates after the network adjustment".

A photograph of the big metal frame taken with *Nikon D100* camera is shown in figure 3-5.

Figure 3-5 3D big metal frame model image.

The targets to be measured appear as white against black metal bar. The space coordinates of the targets on this frame were computed and later used as control and test points for reconstructing the 3D object coordinates from Lodox Statscan X-ray images. The black frame was designed with a series of 76 targets painted white for enhanced contrast in the images. A convergent network of 10 images

incorporating orthogonal roll angle diversity was photographed at close-range. All targets on the images were measured, resection was performed and then a free-net bundle adjustment was executed. The results obtained from the bundle were the 3D space coordinates of the frame targets. The 3D display of the reconstructed target points on the metal frame is shown in figure 3-6.

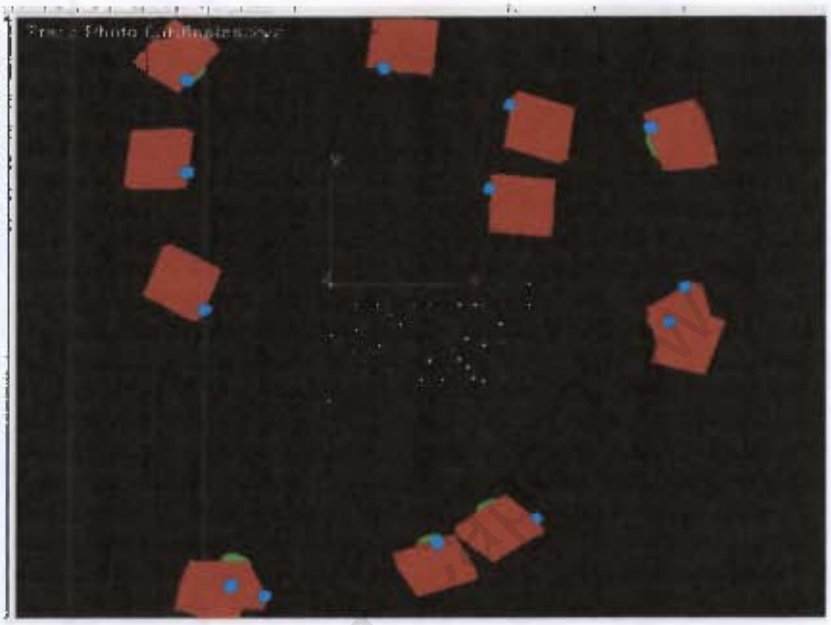

Figure 3-6 Frame graphics showing reconstructed targets and the camera stations within *Australis*.

The reconstructed space coordinates of the big metal frame have been tabulated with point positioning accuracy (see table 3-1).

Point label	Xmm	Ymm	Zmm	Sigma X	Sigma Y	Sigma Z
1	296.9	-1147.9	-281.1	0.4	0.3	0.2
2	201.0	-1139.5	-278.4	0.3	0.2	0.2
3	101.0	-1128.4	-278.5	0.3	0.2	0.1
4	-32.4	-1116.1	-277.3	0.2	0.2	0.1
5	-178.3	-1103.8	-276.9	0.2	0.3	0.1
6	-282.7	-1094.8	-277.2	0.2	0.4	0.1
7	-288.1	-1158.9	-184.9	0.2	0.4	0.1
8	-292.9	-1227.2	-87.3	0.1	0.4	0.1
9	-298.0	-1293.5	5.7	0.1	0.4	0.1
10	-304.0	-1369.0	110.2	0.1	0.4	0.2
11	-308.8	-1432.2	200.8	0.1	0.3	0.2

Point label	Xmm	Ymm	Zmm	Sigma X	Sigma Y	Sigma Z
12	-317.1	-1521.2	325.2	0.1	0.3	0.2
13	-327.7	-1603.6	439.8	0.2	0.3	0.3
14	-177.6	-1615.7	438.7	0.1	0.3	0.2
15	-69.8	-1626.5	438.9	0.1	0.4	0.2
17	256.3	-1661.9	441.4	0.1	0.6	0.1
19	272.0	-1491.2	202.9	0.2	0.5	0.1
20	282.0	-1398.2	70.7	0.2	0.4	0.1
21	287.5	-1315.5	-43.3	0.3	0.4	0.1
22	294.6	-1234.2	-158.4	0.3	0.3	0.2
31	193.0	-1246.9	-106.5	0.3	0.3	0.1
32	15.1	-1230.4	-106.6	0.2	0.2	0.1
33	-189.0	-1209.6	-104.7	0.2	0.3	0.1
34	-212.6	-1485.0	279.8	0.1	0.4	0.2
35	-7.8	-1503.0	276.9	0.1	0.4	0.2
36	166.2	-1520.1	275.7	0.2	0.5	0.1
51	111.4	-1423.3	-155.9	0.1	0.3	0.2
52	-30.6	-1412.8	-153.8	0.1	0.4	0.1
53	-159.7	-1399.6	-152.1	0.1	0.3	0.1
54	-171.9	-1601.4	128.9	0.2	0.5	0.1
56	111.5	-1629.9	127.9	0.1	0.4	0.1
62	-94.6	-1249.0	-225.1	0.1	0.3	0.1
65	-116.8	-1512.7	139.8	0.1	0.3	0.2
66	-124.3	-1606.7	275.4	0.1	0.4	0.2
67	59.0	-1622.2	279.3	0.1	0.4	0.1
68	68.9	-1541.4	150.9	0.2	0.5	0.3
69	73.5	-1455.1	36.9	0.1	0.3	0.1
70	75.6	-1376.8	-72.1	0.1	0.3	0.2
71	175.0	-1342.0	-301.2	0.1	0.3	0.2
72	-4.2	-1323.2	-299.8	0.1	0.2	0.2
73	-202.4	-1305.9	-299.3	0.1	0.3	0.1
74	-206.8	-1383.3	-188.6	0.1	0.3	0.1
75	-210.3	-1424.9	-128.4	0.1	0.3	0.1
76	-216.9	-1497.6	-23.9	0.2	0.3	0.1
77	-220.1	-1540.6	37.8	0.2	0.3	0.1
78	-224.5	-1612.7	136.6	0.2	0.3	0.1
79	-233.6	-1697.8	254.2	0.2	0.3	0.2
80	-102.5	-1709.4	252.1	0.2	0.4	0.1
81	5.9	-1720.9	252.3	0.2	0.4	0.1
82	153.9	-1734.3	249.3	0.1	0.5	0.1
85	167.1	-1557.5	6.9	0.1	0.4	0.1
86	170.6	-1502.9	-70.3	0.1	0.4	0.1
87	175.4	-1425.3	-182.5	0.1	0.3	0.2

Table 3-1 Space coordinates of the big frame target points obtained from *Australis* bundle adjustment.

3.2 PRECISE DIGITAL THEODOLITE METHOD

3.2.1 Determination of 3D frame coordinates

Precise theodolite positioning method was used to determine 3D coordinates of the same big metal frame model. The metal frame was positioned on a table for observation from three theodolite stations (A, B and C). The setup for the theodolite observations on the metal frame is shown in figure 3-7.

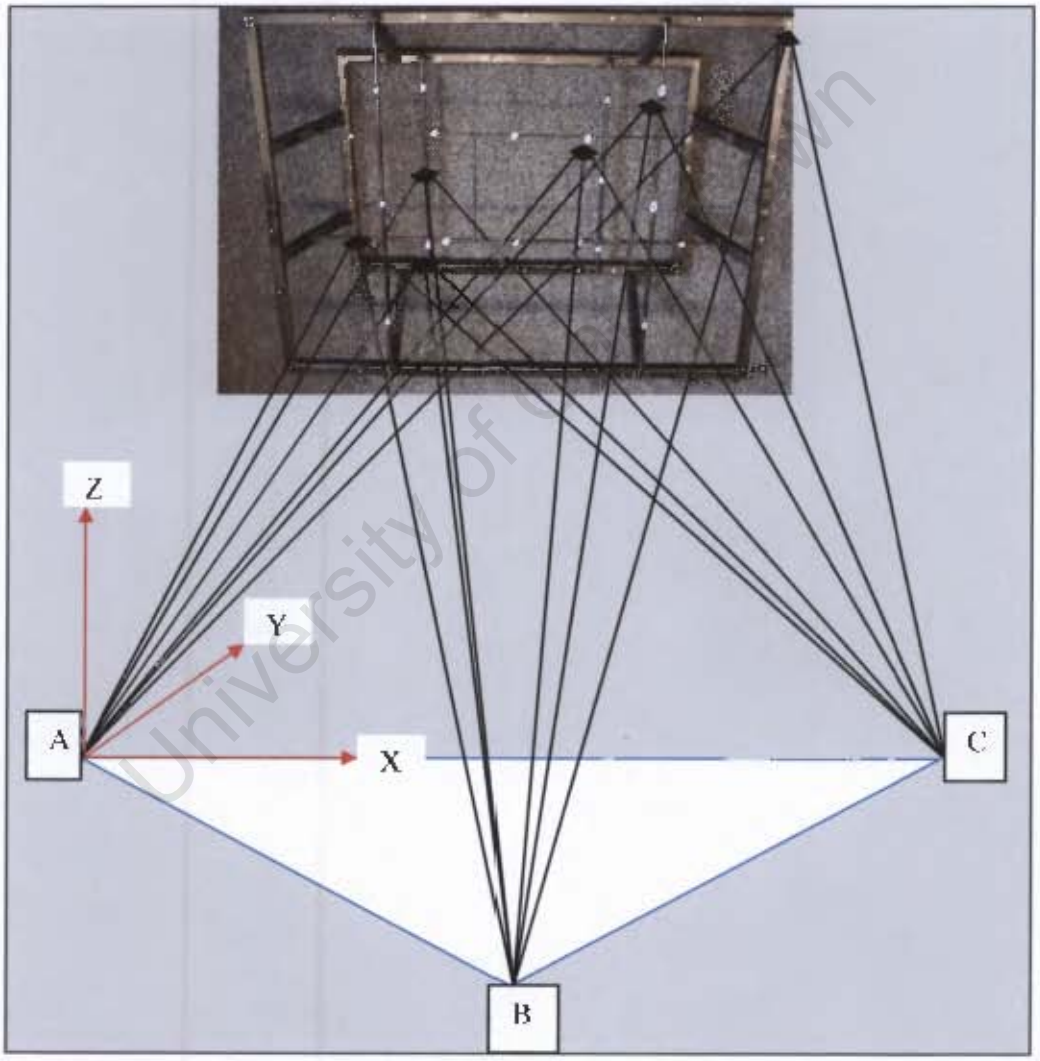

Figure 3-7 Triangulation network from theodolite stations A, B and C

The theodolite stations formed an observation network of triangles to the target points. Forced centering was used with targets placed on two stations and the theodolite on the third station. At every station, horizontal and vertical angles were measured to the other two stations, then to every target point on the frame, and finally back to the stations to check instrument orientation. Prisms were used to electronically measure distances between the theodolite stations to get the baselines. The recorded data was used to compute the provisional point coordinates (x, y) from horizontal angles and distances. These provisional coordinates were adjusted by free network least squares adjustment programme[8] (parametric case) to compute the final planimetric coordinates. The final adjusted x, y-coordinates were used in computing the distances required for the determination of the $z-$coordinates. The observed vertical angles from the control stations to the points were used with the computed distances from the stations to the points. Table 3-2 gives the determined 3D positions of the frame target points.

Point Label	X(mm)	Y(mm)	Z(mm)
1	3787.7	591.4	-718.3
2	3838.3	594.1	-637.3
3	3892.6	594.2	-551.6
4	3965	596.7	-439.4
5	4045.9	599.6	-318.4
6	4103.5	600.8	-231.1
7	4099.3	713.6	-230.1
8	4093.3	832.7	-229.9
9	4089.2	946.7	-229.7
10	4085.7	1075.4	-231.0
11	4080.2	1185.9	-229.9
12	4076.3	1338.9	-228.7
13	4074.4	1479.8	-225.2
14	3991.9	1476.6	-350.3
15	3932.2	1475.9	-441.3

[8] Acknwoledgement to Prof. Rüther, H. of Geomatics (UCT) for providing the least squares programme.

Point Label	X(mm)	Y(mm)	Z(mm)
17	3755.3	1477.6	-717.5
19	3764.3	1183.4	-718.4
20	3768.5	1022.1	-721.5
21	3773.2	881.7	-720.3
22	3778.6	740.7	-721.2
31	3821.1	796.2	-630.5
32	3919.7	798	-481.3
33	4029.2	800.3	-308.9
34	4013.5	1273.8	-307.7
35	3903.5	1268.6	-479.5
36	3808.7	1266.4	-626.1
51	4002.5	869.4	-672.1
52	4079.9	874.1	-554.2
53	4150.2	876.6	-444.4
54	4136.6	1220.4	-447.6
55	4060.8	1220.7	-563.6
56	3983.2	1218.1	-686.1
61	3963.7	724.8	-597.9
62	4056.3	722.5	-442.5
65	4044.7	1173.1	-442.5
66	4034.9	1337.3	-441.0
67	3933	1337.6	-592.6
68	3941.6	1186.5	-599.3
69	3947	1043.8	-596.5
70	3953	910.3	-592.9
72	4085.1	702	-576.2
73	4194.9	705.3	-410.3
74	4187.7	840.1	-410.6
75	4183.9	913.3	-410.1
77	4175.8	1115.5	-408.1
78	4171.8	1237.7	-409.3
79	4169.1	1382.8	-408.3
80	4097.3	1379.3	-518.0
81	4038.9	1379.2	-610.1
82	3959.3	1375	-734.8
85	3966.7	1075	-732.6
87	3978.9	844.3	-732.2

Table 3-2 Adjusted space coordinates of big metal frame target points determined by theodolite method.

3.2.2 3D Coordinate Transformations

The object's local coordinate system was specified to be a right-handed system with the origin coinciding with theodolite station A, and the X-axis horizontal and along AC (see figure 3-7; X-axis and AC are on the same vertical plane). In digital photogrammetry, the first camera station was the origin and the subsequent cameras were oriented relative to the first one. The first step was to convert the two systems into a coordinate system with the same axis orientation. This was accomplished by inverting the y - coordinates of all the target points in the photogrammetric model. The resultant was a right-hand system that was used in all the subsequent 3D transformations. Three-dimensional rigid body transformation of one system to the other preserves the shape of the model. The transformation helps in comparison by providing the discrepancies between the coordinate sets, represented by the residuals (v). Equation (3-3) is used for three-dimensional similarity transformation.

$$\begin{bmatrix} X' \\ Y' \\ Z' \end{bmatrix} = sM \begin{bmatrix} X \\ Y \\ Z \end{bmatrix} + \begin{bmatrix} T_x \\ T_y \\ T_z \end{bmatrix} \qquad (3\text{-}3)$$

where;

s is the scale factor,

M is a 3-by-3 orthogonal rotation matrix,

T_x, T_y and T_z are the translations along the three axes.

The coordinates obtained from theodolite method were transformed into those obtained from digital photogrammetry using the 3D transformation tool of *Australis* software. The final transformation parameters used in the transformation are presented in table 3-3.

Transformation Parameter	Value	Std. Error
Xo (mm)	3125.7	0.37
Yo (mm)	144.2	0.34
Zo (mm)	199.9	0.39
Scale	1.00162	0.00021
Omega	-67.8	0.02
Phi	-30.8	0.01
Kappa	134.9	0.02

Table 3-3 Final rigid body transformation parameters.

The Root Mean Square (RMS) of the XYZ residuals obtained from the transformed coordinates was 0.5 mm. The deduction from these results was that the digital photogrammetric procedure was satisfactorily accurate in determination of space control points that could be used in 3D localization for the Statscan digital X-ray system. The transformed coordinates and the coordinate differences in each point are tabulated in table 3-4.

$$RMS(XYZ) = \sqrt{\frac{\sum\left(DX^2 + DY^2 + DZ^2\right)}{3n}} \qquad (3\text{-}4)$$

Where;

DX, *DY* and *DZ* are residuals in X, Y and Z respectively;

n is the total number of target points.

Point label	Xp	Yp	Zp	Xt	Yt	Zt	DX	DY	DZ
1	296.9	-1147.9	-281.1	296.8	-1148.4	-281.6	0.1	0.5	0.5
2	201.0	-1139.5	-278.4	201.6	-1139	-279	-0.6	-0.5	0.6
3	101.0	-1128.4	-278.5	100.6	-1127.8	-278.9	0.4	-0.6	0.4
4	-32.4	-1116.1	-277.3	-32.6	-1115.4	-277.5	0.2	-0.7	0.2
5	-178.3	-1103.8	-276.9	-178	-1103.8	-277.4	-0.3	0.0	0.5
6	-282.7	-1094.8	-277.2	-282.3	-1094.5	-277.5	-0.4	-0.3	0.3
7	-288.1	-1158.9	-184.9	-288.1	-1159.5	-185.2	0.0	0.6	0.3
8	-292.9	-1227.2	-87.3	-292.6	-1227.6	-87.1	-0.3	0.4	-0.2
9	-298.0	-1293.5	5.7	-297.9	-1293.8	5.9	-0.1	0.3	-0.2
10	-304.0	-1369.0	110.2	-303.3	-1370	109.8	-0.7	1.0	0.4
11	-308.8	-1432.2	200.8	-308.2	-1432.7	201	-0.6	0.5	-0.2
12	-317.1	-1521.2	325.2	-317	-1522	325.3	-0.1	0.8	-0.1
13	-327.7	-1603.6	439.8	-328	-1604.1	439.6	0.3	0.5	0.2
14	-177.6	-1615.7	438.7	-178.4	-1616.6	438.7	0.8	0.9	0.0
15	-69.8	-1626.5	438.9	-69.9	-1626.8	439.1	0.1	0.3	-0.2
17	256.3	-1661.9	441.4	256.6	-1662.9	441.4	-0.3	1.0	0.0
19	272.0	-1491.2	202.9	271.5	-1491.3	202.1	0.5	0.1	0.8
20	282.0	-1398.2	70.7	282.2	-1398.2	70.4	-0.2	0.0	0.3
21	287.5	-1315.5	-43.3	287.8	-1315.7	-43.5	-0.3	0.2	0.2
22	294.6	-1234.2	-158.4	294.6	-1234.4	-158.9	0.0	0.2	0.5
31	193.0	-1246.9	-106.5	193.2	-1246.9	-107	-0.2	0.0	0.5
32	15.1	-1230.4	-106.6	14.7	-1230.9	-107.6	0.4	0.5	1.0
33	-189.0	-1209.6	-104.7	-188.7	-1209.9	-105.8	-0.3	0.3	1.1
34	-212.6	-1485.0	279.8	-211.8	-1485.3	279.9	-0.8	0.3	-0.1
35	-7.8	-1503.0	276.9	-8.3	-1504	276.3	0.5	1.0	0.6
36	166.2	-1520.1	275.7	165.8	-1520.7	275.4	0.4	0.6	0.3
51	111.4	-1423.3	-155.9	111.1	-1423.1	-155.2	0.3	-0.2	-0.7
52	-30.6	-1412.8	-153.8	-29.8	-1412.2	-152.7	-0.8	-0.6	-1.1
53	-159.7	-1399.6	-152.1	-159.8	-1399.7	-151.1	0.1	0.1	-1.0
54	-171.9	-1601.4	128.9	-172	-1600.5	128.8	0.1	-0.9	0.1
56	111.5	-1629.9	127.9	110.6	-1629	128	0.9	-0.9	-0.1
62	-94.6	-1249.0	-225.1	-94	-1248.5	-225.1	-0.6	-0.5	0.0
65	-116.8	-1512.7	139.8	-117	-1513.3	139.8	0.2	0.6	0.0
66	-124.3	-1606.7	275.4	-123.2	-1605.7	276.2	-1.1	-1.0	-0.8
67	59.0	-1622.2	279.3	59	-1622.1	279.3	0.0	-0.1	0.0
68	68.9	-1541.4	150.9	69.1	-1539.7	152.4	-0.2	-1.7	-1.5
69	73.5	-1455.1	36.9	73.1	-1455.4	36.8	0.4	0.3	0.1
70	75.6	-1376.8	-72.1	75.6	-1376.7	-71.4	0.0	-0.1	-0.7
72	-4.2	-1323.2	-299.8	-4	-1322.9	-299.7	-0.2	-0.3	-0.1
73	-202.4	-1305.9	-299.3	-202.6	-1306	-299.4	0.2	0.1	0.1
74	-206.8	-1383.3	-188.6	-207	-1383.1	-188.4	0.2	-0.2	-0.2
75	-210.3	-1424.9	-128.4	-210	-1424.7	-128	-0.3	-0.2	-0.4
77	-220.1	-1540.6	37.8	-220.1	-1540.7	37.9	0.0	0.1	-0.1
78	-224.5	-1612.7	136.6	-224.9	-1612.6	137	0.4	-0.1	-0.4
79	-233.6	-1697.8	254.2	-233.8	-1698	254.3	0.2	0.2	-0.1
80	-102.5	-1709.4	252.1	-102.8	-1708.9	252.6	0.3	-0.5	-0.5
81	5.9	-1720.9	252.3	5.7	-1720.8	252.5	0.2	-0.1	-0.2
82	153.9	-1734.3	249.3	153.4	-1734.3	249.4	0.5	0.0	-0.1
85	167.1	-1557.5	6.9	167.1	-1556.6	7.3	0.0	-0.9	-0.4
87	175.4	-1425.3	-182.5	174.8	-1424.7	-182.6	0.6	-0.6	0.1
							RMS(XYZ)=0.5mm		

Table 3-4 Comparison between transformed theodolite coordinates (*Xt, Yt, Zt*) into Photo coordinates (*Xp, Yp, Zp*).

In the case of the small metal frame, the digital photogrammetry method was used to determine the space control coordinates for all the target points. The theodolite observations were only done on the big metal frame to compare the accuracy obtained and to choose one method to be used in the X-Ray reconstruction. The small frame has one set of control coordinates obtained from digital photogrammetry method, therefore no comparison has been done as is the case in the big metal frame. Since the comparison done using coordinates from the big metal frame was found to give satisfactory accuracy, this procedure was not repeated on the small metal frame. The space control points of the small metal frame obtained from digital photogrammetry are given in table 3-5 below:-

Point Label	X (mm)	Y (mm)	Z (mm)	Sigma X	Sigma Y	Sigma Z
1	98.6	98.5	-0.3	0.3	0.3	0.4
2	98.5	313.7	3.2	0.3	0.3	0.5
3	147.4	98.7	2.3	0.2	0.3	0.4
4	146.8	206.8	6.8	0.2	0.2	0.4
5	148.4	313.9	5.1	0.3	0.3	0.5
6	208.7	97.6	3.2	0.2	0.3	0.4
7	208.9	207.4	6.7	0.2	0.2	0.4
8	208.4	314.5	3.9	0.2	0.2	0.4
9	267.8	98.3	2.7	0.2	0.3	0.4
10	267.9	208.0	6.0	0.2	0.2	0.4
11	268.2	315.4	3.3	0.2	0.2	0.4
12	316.9	99.2	0.7	0.3	0.2	0.4
13	316.4	316.2	0.9	0.3	0.3	0.5
14	140.6	93.6	269.5	0.2	0.3	0.4
15	139.3	206.0	268.6	0.2	0.2	0.3
16	138.4	318.1	267.6	0.2	0.3	0.3
17	207.9	95.0	269.8	0.2	0.2	0.4
18	207.7	206.6	269.3	0.2	0.2	0.3
19	206.4	320.1	268.0	0.2	0.3	0.3
20	276.4	95.5	270.8	0.2	0.2	0.4
21	275.0	208.0	270.0	0.2	0.2	0.3
22	274.6	321.0	268.3	0.2	0.3	0.3

Table 3-5 Space coordinates of the small metal frame target points obtained from *Australis* bundle adjustment.

CHAPTER FOUR

4.0 THREE-DIMENSIONAL RECONSTRUCTION OF POINTS FROM LODOX STATSCAN X-RAY IMAGES

4.1 SCANNING TECHNOLOGY OF STATSCAN X-RAY SYSTEM

The Statscan digital X-ray system scans in a linear slit/slot scanning motion. The objects to be scanned lie motionless on the platform, while the C-arm bearing the X-ray tube and the digital detector moves along the platform. The C-arm can rotate laterally up to 90 degrees thus enabling the acquisition of object images at different orientation. The digital detector that consists of a screen, optically coupled by fiber optic taper (FOT), to twelve scientific grade CCD's operated in time delay integration (TDI) mode, lie directly beneath the platform and aligned with the X-ray source. ' See http://www.lodox.com/ '. Figure 4-1 shows the labeled parts of Statscan imaging system.

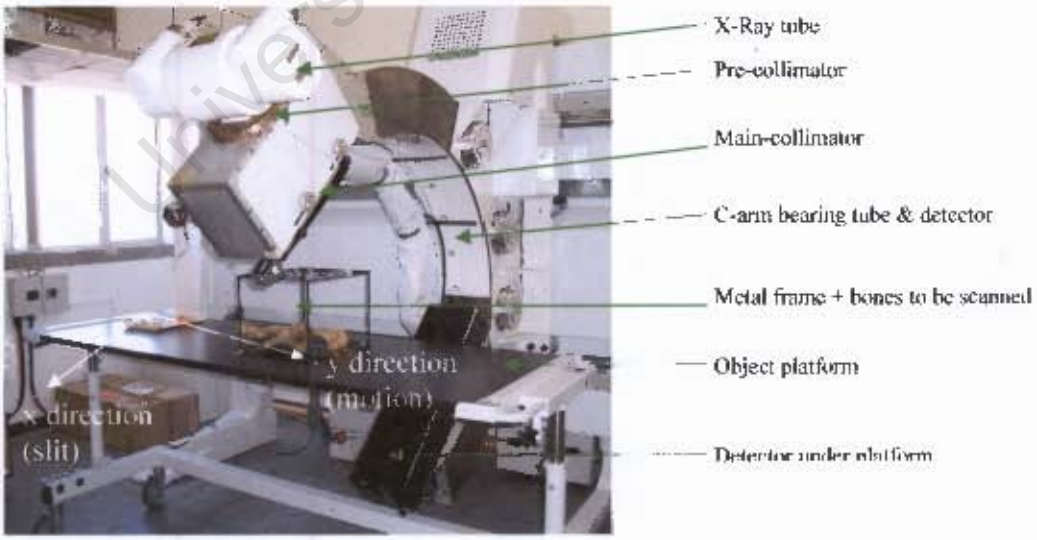

Figure 4-1 Labeled parts of the Lodox Statscan system.

In the Statscan linear slit scanning, the image is acquired at a multitude of points along the scan line. The resulting geometry is line perspective geometry similar to that of satellite pushbroom sensor, as shown in figure 4-2, as opposed to the general central perspective geometry of the conventional X-ray modality. A single image consists of a number of consecutive scan lines. Each line has its own time-dependent position and exterior orientation parameters. In order for the image to have a stable geometry suitable for photogrammetric analysis, it is essential that the C-arm carrying the X-ray tube and the linear array sensor moves smoothly as the image is acquired. However, a constant motion remains an ideal case due to the mechanical movement of joint parts and vibrations caused by the X-ray tube. If the sensor tips and tilts erratically, as the images are being acquired, the resulting image gets correspondingly distorted.

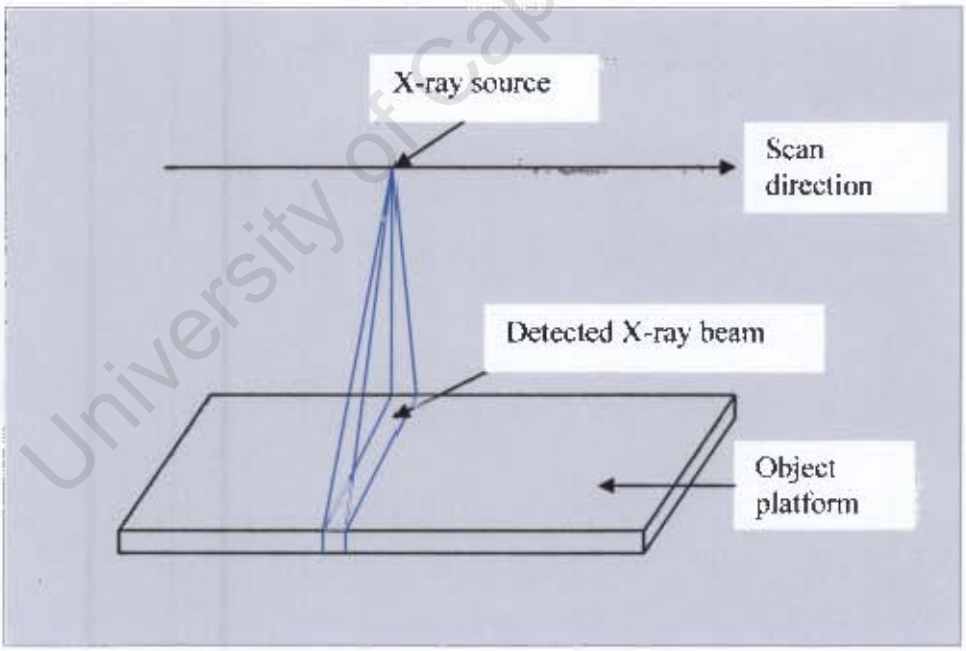

Figure 4-2 Schematic of the X-ray linear scanning.

The platform on which the object is placed for scanning is 700mm wide at the detector section. A narrow vertical X-ray beam (3-6mm*700mm) scans along the platform. The beam shape is set by two narrow slits (collimators) before getting to the object and a post collimator directs the beam to the detector through the scintillator. The post collimator blocks any scattered radiation outside the primary main beam. The X-ray scan direction along the platform gives the $y-$ component of the image while the beam slit across the platform is taken as $x-$direction, as used in defining the coordinate system.

It has been reported that in slit scanning systems, the tube output fluctuations and scan speed variations introduce banding in the scan direction. In order to reduce such effects, the C-arm has been designed to dampen anode vibration and the linear drive induction motor chosen to allow a high degree of scan speed accuracy. The X-ray tube is mounted with the plane of the rotating anode in the slit direction, thus the slit opens to a very narrow portion of the beam. For further image processing, Lodox has introduced image enhancement tool known as Lucid. When the Lucid tool is used on X-ray images, it automatically displays detailed contrast of the structures being imaged. This is achieved by automatic adjustment of the grey scale window and level for optimal image viewing. 'See http://www.lodox.com/html/lucid.html '.

The Statscan setup for image acquisition determines the amount of data that can be extracted from an output image. Change of orientation angle by rotating the Statscan C-arm in between subsequent scans has produced multiple experimental data (see figure 4-3).

Figure 4-3 Lodox Statscan System at frontal position (left), near mid angle rotation (middle) and C-arm rotated to capture lateral image (right)[9]

A scan velocity of 140 mm/s was set and several images scanned at 1.39 lp/mm resolution. The instantaneous imaging rate of the Statscan was 22-88 milliseconds. The instantaneous imaging rate gives a measure of the time taken for the X-ray beam to traverse a particular point, which can also be explained as the point exposure time.

[9] Diagram sourced from http://www.lodox.com/

(a)

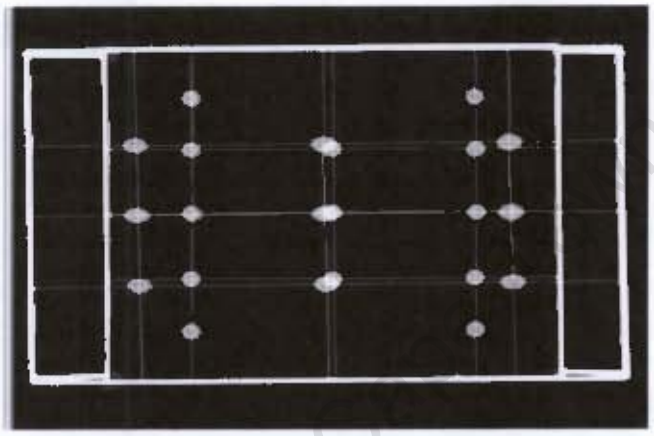

(b)

Figure 4-4 Photo image of the small metal frame on the X-ray scanning platform (a) and the digital image output (b) from AP imaging position.

4.1.1 Image preparation for measurements

The images acquired using Statscan were exported in Bitmap format that can be supported by *Matlab* software and Microsoft photo manager. *Matlab* was used to measure image sizes. The image size was measured by reading the Windows Bitmap image file in *Matlab* workspace. For images found to be of different sizes, image cropping was done using Microsoft photo manager. The cropping reduced equal number of pixels from top and bottom of the image, thus preserving the perspective centre of the image. The images obtained on the Statscan image platform were

of slightly different sizes because of manual selection of the start point for each scan. Cropping was done in order to enable image coordinate measurement by *Australis* software. The *Australis* project data file imports images of the same size and resolution at once.

4.1.2 Image Coordinate Measurements

The X-ray images from Lodox Statscan were imported to PC-based *Australis* software in Bitmap format where image coordinates were measured. The control points were selected from the determined points, and used in varying combinations to test the network strength. The measurements were accomplished and x and y coordinates for each image recorded. These image coordinates were used in different experiments to investigate the point positioning accuracy in three-dimensional space.

4.2 THREE-DIMENSIONAL RECONSTRUCTION USING STATSCAN IMAGES

The Lodox Statscan object space coordinates were computed through a transformation from 2D X-ray image coordinates into 3D control object space coordinates. The control and test space coordinates obtained from digital photogrammetry were used in Direct Linear Transformation (DLT). The measured image coordinates were exported into Direct Linear Transformation (DLT)[10] code for three-dimensional point reconstruction. The DLT method has been used in research at the University of Cape Town, Department of Biomedical Engineering and Geomatics Division for years (see e.g. Adams (1981), Van Geems (1995), Douglas (2004), Rüther (2005)). Iterative least squares solution

[10] Acknowledgement to Rudolf Neeser of Heritage Research Group (UCT) for coding standard DLT in C++, James Parkes of Geomatics (UCT) for coding DLT in Visual Basic and Indresan Govender of CERECAM (UCT) for providing standard DLT test code in Matlab.

was implemented to determine the DLT parameters. The standard DLT equations used for transforming image coordinates x and y into the object coordinates X,Y and Z can be written as shown in equation 4-1. Six control points are identified distributed on the corners and inside the metal frame.

The control coordinates previously determined (table 3-1) were used, and the image coordinates for the control points applied in equation 4-1 to solve for the 11 DLT parameters. Once the parameters were calculated, they were substituted in the DLT equation and a solution for the test coordinates was obtained. The precision of the DLT terms, which is an internal measure of accuracy, was obtained by computing the variance-covariance matrix of the determined DLT parameters. In order to check the external accuracy in 3D localization, the space coordinates were compared to those obtained by digital photogrammetry. Accuracy, the measure of agreement between the observed and photogrammetric X,Y and Z coordinates was computed. The least squares solution was executed iteratively to compute the values for the DLT parameters; (L_1) through (L_{11}).

4.2.1 Solving for the 11 DLT parameters

Marzan and Karara (1976) wrote the first DLT computer program for transforming comparator coordinates to object coordinates. The mathematical derivations by Marzan and Karara have been adopted for the Lodox statscan 3D localization. The standard DLT equations are given as:-

$$\left.\begin{aligned} x &= \frac{L_1X + L_2Y + L_3Z + L_4}{L_9X + L_{10}Y + L_{11}Z + 1} \\ y &= \frac{L_5X + L_6Y + L_7Z + L_8}{L_9X + L_{10}Y + L_{11}Z + 1} \end{aligned}\right\} \qquad (4\text{-}1)$$

where;

$L_1 - L_{11}$ are the transformation parameters,

x, y are the image coordinates,

X, Y, Z are the control coordinates.

Equation 4-1 can be rewritten in a linear form as:

$$\left.\begin{aligned} F_x &= x(L_9X + L_{10}Y + L_{11}Z + 1) - (L_1X + L_2Y + L_3Z + L_4) = 0 \\ F_y &= y(L_9X + L_{10}Y + L_{11}Z + 1) - (L_5X + L_6Y + L_7Z + L_8) = 0 \end{aligned}\right\} \quad (4\text{-}2)$$

The Statscan imaging system does not make use of a camera with lenses, which would generate systematic errors from lens distortion. The principal point coordinates (x_p, y_p) and principal distances in x and y coordinate direction (c_x, c_y), were computed after the solution for the 11 parameters was obtained. An algebraic solution of the DLT solution yields the camera parameters as follows (Karara, 1979):

$$
\left.
\begin{aligned}
L &= \frac{-1}{\sqrt{\left(L_9^{\,2} + L_{10}^{\,2} + L_{11}^{\,2}\right)}} \\
x_p &= \left(L_1 L_9 + L_2 L_{10} + L_3 L_{11}\right) L^2 \\
y_p &= \left(L_5 L_9 + L_6 L_{10} + L_7 L_{11}\right) L^2 \\
c_x &= \sqrt{\left[\left(L_1^{\,2} + L_2^{\,2} + L_3^{\,2}\right) L^2 - x_p^{\,2}\right]} \\
c_y &= \sqrt{\left[\left(L_5^{\,2} + L_6^{\,2} + L_7^{\,2}\right) L^2 - y_p^{\,2}\right]} \\
\varphi &= \sin^{-1}\left(L_9 L\right) \\
\omega &= \tan^{-1}\left(\frac{-L_{10}}{L_{11}}\right) \\
m_{11} &= \frac{L\left(x_p L_9 - L_1\right)}{c_x} \\
\kappa &= \frac{\cos^{-1}\left(m_{11}\right)}{\cos\varphi}
\end{aligned}
\right\} \qquad (4\text{-}3)
$$

The pair of observation equations written for each observed point is;

$$V_i + B_i \Delta_j + D_i = 0 \qquad (4\text{-}4)$$

where;

$$V_i = \begin{bmatrix} v_{x_i} \\ v_{y_i} \end{bmatrix} \qquad (4\text{-}5)$$

$$B_i = \begin{bmatrix} -X & -Y & -Z & -1 & 0 & 0 & 0 & 0 & xX & xY & xZ \\ 0 & 0 & 0 & 0 & -X & -Y & -Z & -1 & yX & yY & yZ \end{bmatrix} \qquad (4\text{-}6)$$

$$\Delta_j^{\,T} = \begin{bmatrix} L_1 & L_2 & L_3 & L_4 & L_5 & L_6 & L_7 & L_8 & L_9 & L_{10} & L_{11} \end{bmatrix}_j \qquad (4\text{-}7)$$

$$D_i = \begin{bmatrix} x_i \\ y_i \end{bmatrix} \qquad (4\text{-}8)$$

By solving equation 4-2 iteratively, D_i in equation 4-4 becomes;

$$\left.\begin{aligned} D_{xi} &= x_i - x_i((L_9X + L_{10}Y + L_{11}Z + 1) - (L_1X + L_2Y + L_3Z + L_4))|_0 = 0 \\ D_{yi} &= y_i - y_i((L_9X + L_{10}Y + L_{11}Z + 1) - (L_5X + L_6Y + L_7Z + L_8))|_0 = 0 \end{aligned}\right\} \quad (4\text{-}9)$$

For n observations, we therefore have in matrix form;

$$\begin{bmatrix} v_{x_1} \\ v_{y_1} \\ v_{x_2} \\ v_{y_2} \\ . \\ . \\ . \\ V_n \end{bmatrix} + \begin{bmatrix} B_{x_1} \\ B_{y_1} \\ B_{x_2} \\ B_{y_2} \\ . \\ . \\ . \\ B_n \end{bmatrix}_2 \Delta_j + \begin{bmatrix} D_{x_1} \\ D_{y_1} \\ D_{x_2} \\ D_{y_2} \\ . \\ . \\ . \\ D_n \end{bmatrix} = 0 \quad (4\text{-}10)$$

The parametric case least squares solution generates the unknown 11 DLT parameters for each image in the reconstruction as;

$$\left.\begin{aligned} \Delta_j &= -\left[B^T B\right]^{-1} B^T D \\ \Delta_j &= -N^{-1} D^* = -Q_{XX} D^* \end{aligned}\right\} \quad (4\text{-}11)$$

where;

$$N = B^T B \text{ and } D^* = B^T D \quad (4\text{-}12)$$

From equation 4-5 the residuals are obtained as;

$$V = -B\Delta_j - D \quad (4\text{-}13)$$

A posteriori variance of unit weight can be computed as;

$$\sigma_0^2 = \frac{V^T V}{df} \tag{4-14}$$

where;

df = number of degrees of freedom in the solution (2n-u),

n is the number of control points used,

u is the number of unknowns to be solved for in the solution.

The equation for the variance-covariance matrix of unknowns will be;

$$\Sigma_{xx} = \sigma^2 Q_{XX} \tag{4-15}$$

4.2.2 Computation of the object space coordinates

Marzan and Karara continue to derive the equations for the determination of new points in object space as follows. The DLT equations have the form;

$$\left.\begin{aligned} x(L_9X + L_{10}Y + L_{11}Z + 1) - (L_1X + L_2Y + L_3Z + L_4) = 0 \\ y(L_9X + L_{10}Y + L_{11}Z + 1) - (L_5X + L_6Y + L_7Z + L_8) = 0 \end{aligned}\right\} \tag{4-16a}$$

or;

$$\left.\begin{aligned} (xL_9 - L_1)X + (xL_{10} - L_2)Y + (xL_{11} - L_3)Z + (x - L_4) = 0 \\ (yL_9 - L_5)X + (yL_{10} - L_6)Y + (yL_{11} - L_7)Z + (y - L_8) = 0 \end{aligned}\right\} \tag{4-16b}$$

Each image used gives one set of equations (4-10b) per point. For p number of images used in the solution, we have $2p$ number of equations to compute for the unknowns X,Y and Z object space coordinates of a target point. The number of degrees of freedom will be;

$$df = 2p - 3 \tag{4-17}$$

The matrix notation for the pair of condition equations used to solve for a point i, in one image j, is written as;

$$V_j + B_j \Delta_i + C_j = 0 \tag{4-18}$$

where;

$$V_j = \begin{bmatrix} v_x \\ v_y \end{bmatrix} \tag{4-19}$$

$$\Delta_i = \begin{bmatrix} X \\ Y \\ Z \end{bmatrix} \tag{4-20}$$

$$B_j = \begin{bmatrix} (xL_9 - L_1) & (xL_{10} - L_2) & (xL_{11} - L_3) \\ (yL_9 - L_5) & (yL_{10} - L_6) & (yL_{11} - L_7) \end{bmatrix} \tag{4-21}$$

$$B_j^T = \begin{bmatrix} (xL_9 - L_1) & (yL_9 - L_5) \\ (xL_{10} - L_2) & (yL_{10} - L_6) \\ (xL_{11} - L_3) & (yL_{11} - L_7) \end{bmatrix} \tag{4-22}$$

$$C_j = \begin{bmatrix} x - L_4 \\ y - L_8 \end{bmatrix} \tag{4-23}$$

The iterative least squares functional model can be expressed as follows;

$$\Delta_i = -\left[B^T B\right]^{-1} B^T C$$

$$= -N^{-1} C^* \tag{4-24}$$

where;

$$\begin{aligned} N &= B^T B \\ C^* &= B^T C \end{aligned} \tag{4-25}$$

The variance of unit weight will as shown above will be;

$$\sigma^2 = \frac{V^T V}{df} \tag{4-26}$$

The variance-covariance matrix of the computed three dimensional space coordinates will therefore be given by the equation;

$$\Sigma_{XX} = \sigma^2 N^{-1} = \sigma^2 Q_{XX} \tag{4-27}$$

The three versions of the DLT algorithm used to perform the object reconstruction from Statscan images were written in the C++ programming language (DLT Version 1.0); (see acknowledgements on page 49), Microsoft *Visual Basic* (DLT Version 1.1) and *Matlab Mathworks* (11_parameter DLT). The final results were computed using the *Visual Basic* version coded by James Parkes of Geomatics (UCT), and plotted in *Matlab* for visualization. In order to solve for the parameters L_1 through L_{11} , at least two images and up to eighteen images in the solution were used. By applying DLT, a solution for the 3D space coordinates of the points of interest was obtained. The flow chart in figure (4-5) is a simplified explanation of the steps for DLT execution.

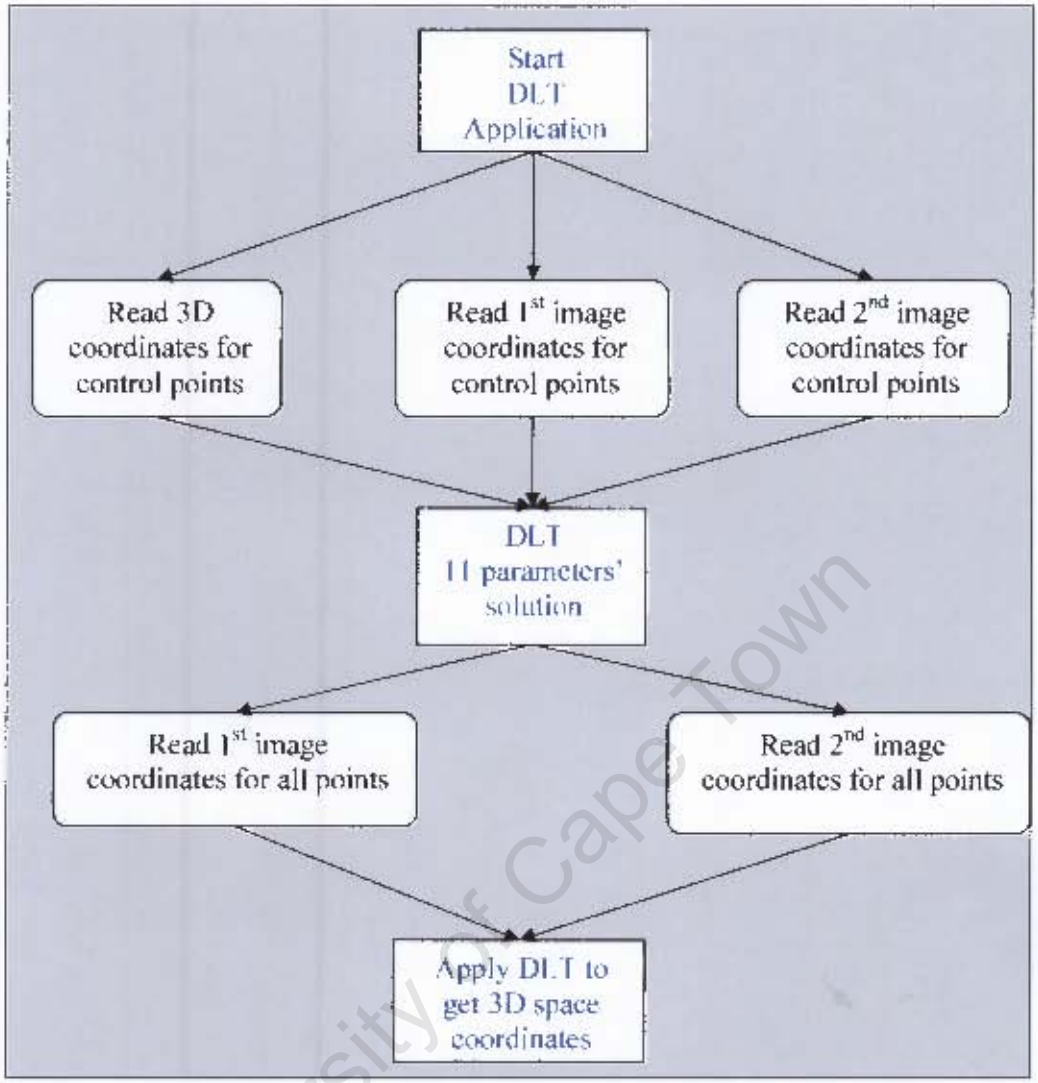

Figure 4-5 Outlined steps for executing the 11 parameter DLT algorithm.

4.2.3 Determination of configuration of object space control points for DLT

The precision of the estimated DLT parameters is affected by both geometric configuration of the object space control points, and stochastic influences. Faig and Shih (1986) reported that, 'the numerical conditions for the normal equation matrix for DLT is influenced by geometric parameters in both image and object space'. Faig and Shih's tests for evaluating the numerical conditions involved investigating:-

- number and geometry of object points;
- ratio of focal length to object distance;
- Object space-camera geometry;
- depth of object.

Faig and Shih stated the following points in their analysis of the test results from simulated data:-

1. The increase in the number of points does not improve the numerical condition, but improves the reliability condition statistically.
2. The larger the translation from the center of gravity to the origin, the larger the condition number for the normal equation matrix, thus poor numerical condition.
3. The absolute photo scale determines the resolution of the image space, thus affecting the precision and resolution of the whole system. The best results have been reported to be achieved when scale ration is unity.
4. The field angle has no effect at the resection stage.
5. The depth problem has been said to be the mutual ratio between 3D magnitudes of object coordinates (i.e. the ratio in object's X, Y and Z). The cube is the optimum configuration.

In order to investigate the number of control points to be used in Statscan reconstruction, a minimum number of six points was chosen

first. Different configuration of the points was experimented. An increased number of the object control points were found not to increase the precision. In fact when the control points were increased from six to ten, the precision became slightly worse, depending on positions and configuration of selected points. This phenomenon was not investigated further as Faig and Shih (1986) had reported that the increase in the number of points does not improve the numerical condition. The minimum number of six points distributed at the corner of frames was used in all ensuing experiments. The investigation done by Faig and Shih (1986) explains the precision achieved in the determination of the DLT parameters used to localize the points in 3D. By studying the trend in the variances extracted from the variance-covariance matrix, a further understanding of DLT approach has been sought.

When images taken from varying orientations were used, the precision increased up to an optimal orientation, and then deteriorated. Faig and Shih stated that the problem of depth is not related to the geometrical arrangement that includes the camera station. The depth depends on the dimension ratios of the object itself, and is not controlled by the relation between object and image. Numerically, a unit ratio between coordinate differences in all the three directions in object space provides the best solution, although it is not always possible to achieve in most experiments due to optical and physical restrictions.

The findings by Faig and Shih do not agree with the results obtained in this investigation, where varying image orientations led to different precision in each case. When the X-ray tube was tilted to obtain images at varying orientations, the image depth was increased to an optimal ratio between the 3D magnitudes of the images' X, *Y* and *Z*. This resulted in increased precision up to the optimal point. Beyond this optimal point, the ratio in image X, Y and Z ratios decreased, leading to deterioration in precision.

CHAPTER FIVE

5.0 PRESENTATION OF EXPERIMENTAL RESULTS, DATA VISUALIZATION AND ANALYSIS

5.1 3D LOCALIZATION USING IMAGES OF TWO DIFFERENT CONTROL POINT DISTRIBUTIONS

The frame images scanned with the Statscan system were used to obtain a solution for the 3D localization of the visible distinct targets on each metal frame. In every experiment, at least two images were combined at a time to solve for the point positions in 3D space. The first image taken at frontal position was used with every other subsequent image. The angle between the images increased progressively. The experiments tested the change in positioning accuracy with increase in convergence angle.

A total of twenty two target points on the small frame were reconstructed from scanned images. The six target points chosen as control points on the small frame were points 1, 2, 12, 13, 14 and 22 (see display on figure 5-8). In the case of the big metal frame, most of the targets were not visible due to the limitation in the imaging geometry of the scanner. Out of the total seventy six targets on the big frame, only twenty three could be measured, and even less in some images. The points chosen as control points on the big frame were 2, 4, 67, 72, 74 and 81.

The root mean square errors in localization of target points on both frames were derived by comparison with the control coordinates established by digital photogrammetry method. The RMS values were

computed and plotted in graphs for visualization. Table 5-1 gives all the images used in the different experiments. The metal frames were scanned by manually selecting the scan angle that rotated the X-ray tube along the Statscan's C-arm. The targets on the big frame images obtained at scan angles beyond 53 degrees could not be measured. Figure 5-1 shows a sketch of the Statscan's C-arm and some X-ray scan orientations.

Object	Images scanned with Statscan (degrees)
Big metal frame	5^0, 9^0, 14^0, 18^0, 22^0 , 26^0, 30^0, 34^0, 39^0, 43^0, 45^0 , 49^0 ,53^0
Small metal frame	Set 1: 0^0, 5^0, 9^0, 14^0, 18^0, 22^0, 26^0, 30^0, 34^0, 39^0, 43^0, 45^0, 49^0, 53^0 Set 2: 0^0, 4^0, 10^0, 15^0, 20^0, 24^0, 30^0, 34^0, 40^0, 45^0, 50^0, 55^0, 60^0, 65^0 , 69^0, 74^0, 84^0, 90^0

Table 5-1 Metal frame images used in Statscan 3D point localization

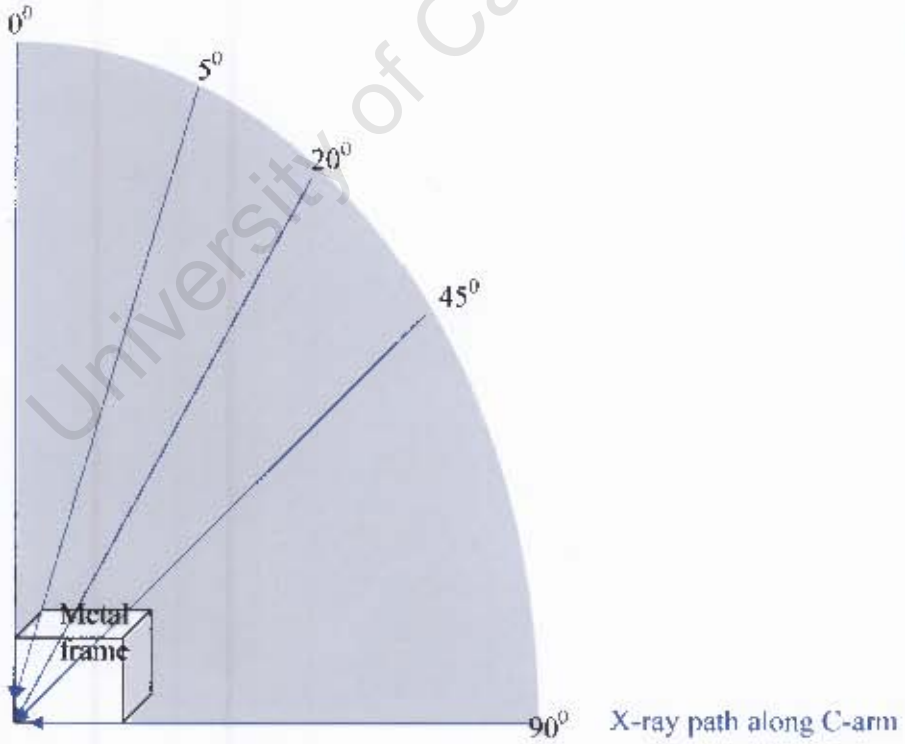

Figure 5-1 Schematic of different X-ray scan orientation angles along the Statscan's C-arm.

5.1.1 Error analysis of the computed DLT parameters

Internal accuracy in determination of DLT parameters from different images was computed from the variances. The results obtained from computing the variance-covariance matrix of the L parameters have been displayed graphically. The variances obtained for L_4 and L_8 have been found to be of very high magnitude as compared to the variances of the other parameters. The L terms vary greatly and therefore the standard deviations are expressed as percentage of the respective DLT parameters. The values for some parameters are very small and hence appear as zeros in the tabulated results. The standard deviations for the determined L_9, L_{10} and L_{11} DLT parameters are quite small and they appear as zero in the tabulated results. Such parameters have been omitted in the graphical representation of internal accuracies in the determined parameters as shown in figure 5-2(a) for the big frame and 5-2(b) for the small frame. The point positioning accuracy depends on the precision in the determination of DLT parameters, and also the combination of images in the DLT solution.

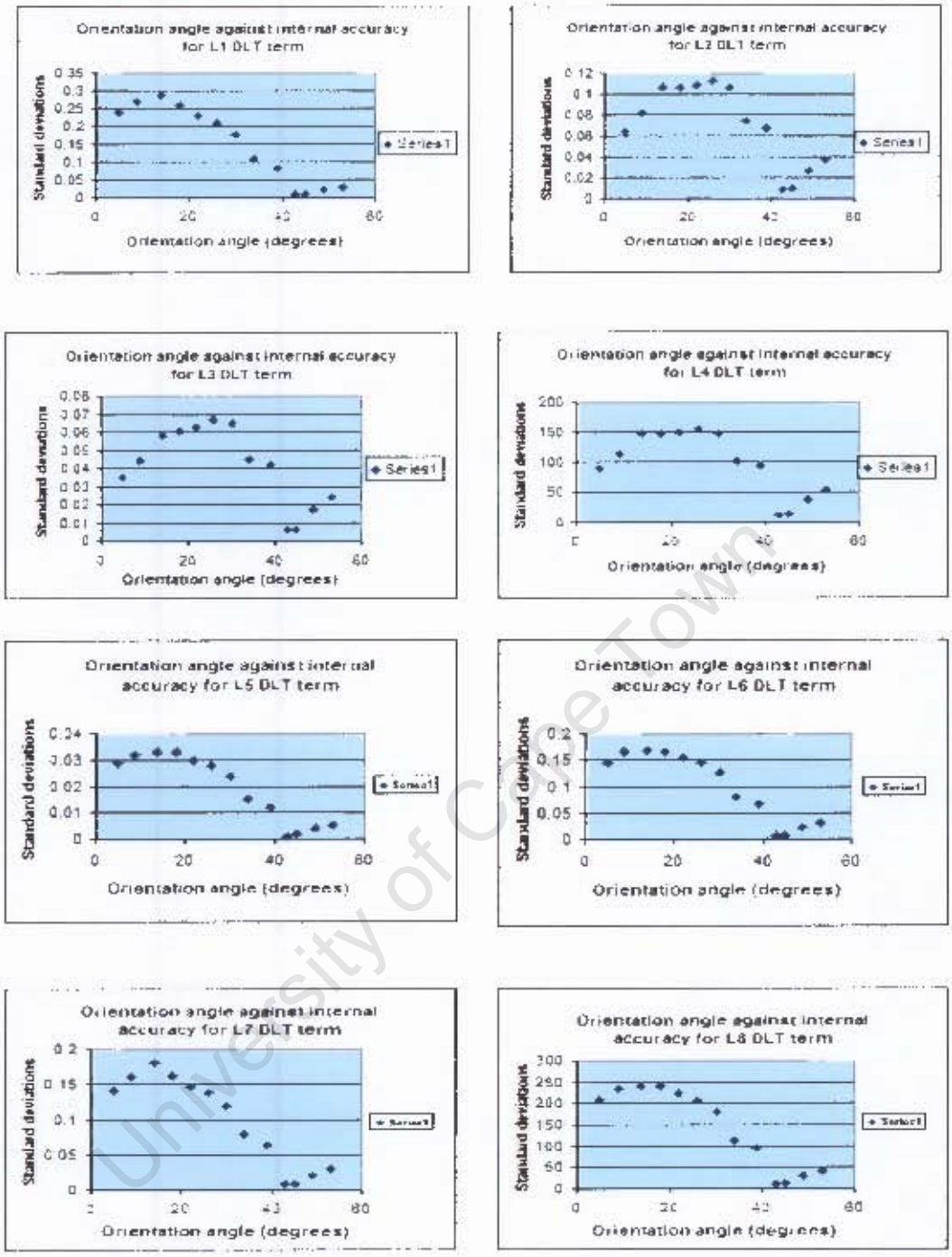

Figure 5-2 (a) Big frame internal accuracies for determined L_1 through L_8 DLT terms.

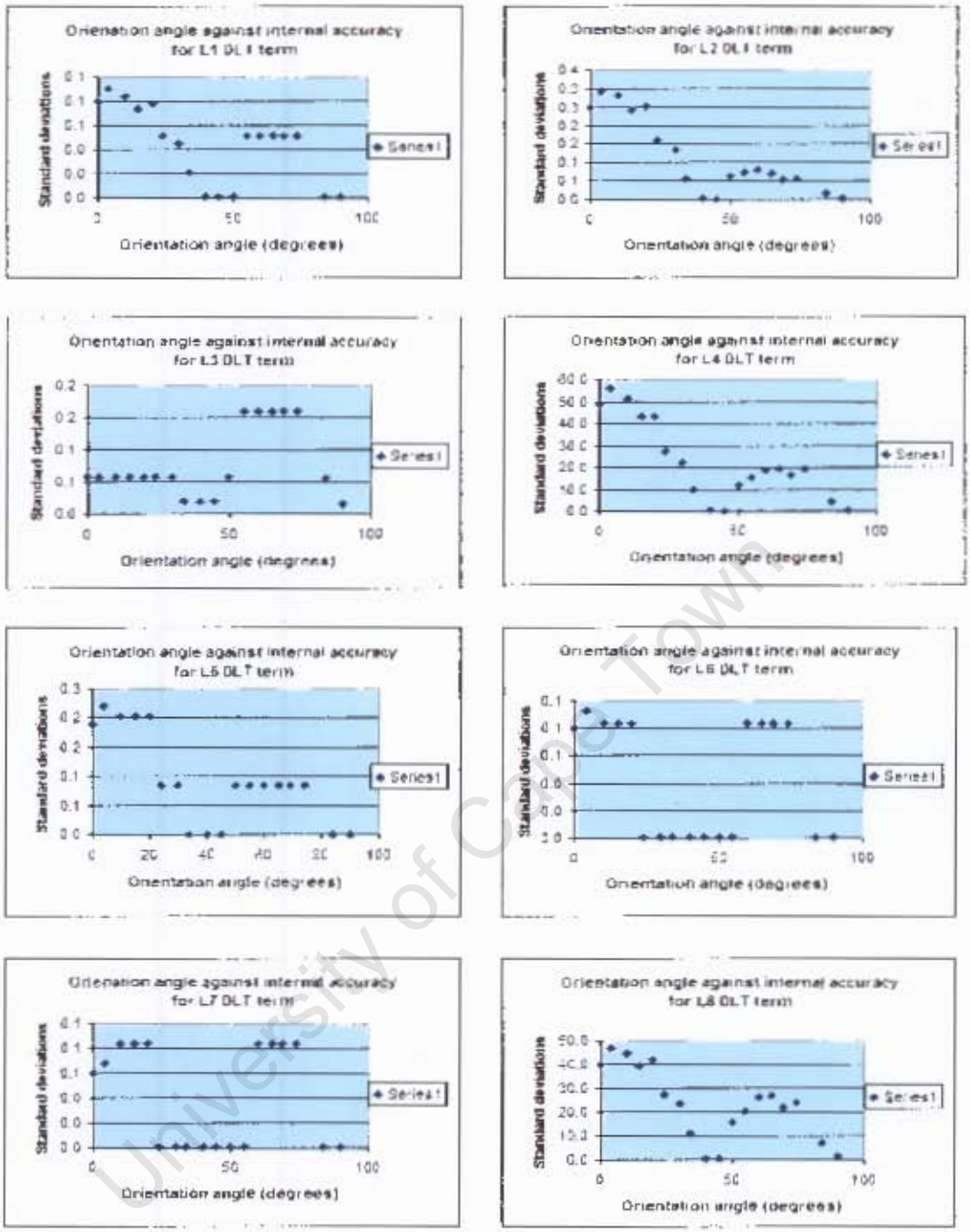

Figure 5-2 (b) Small frame internal accuracies for determined L_1 through L_8 DLT terms.

5.1.2 Reconstruction of the big frame

The experiments were designed to study the change in attainable point positioning accuracy with progressive image convergence angles. The first image was taken at 5 degrees, and this image was combined with each other image taken after moving the X-ray tube. Image coordinates for all the scans were measured. Two images were used at a time in the DLT algorithm and point positioning accuracy was computed for each case. Six points {2, 4, 67, 72, 74 and 81} at the extremes and inside of the metal frame were chosen as control. The dimensions of the big metal frame are 900mm*600mm*205mm. Figure 5-3 shows the measured targets on 14 degree Statscan image.

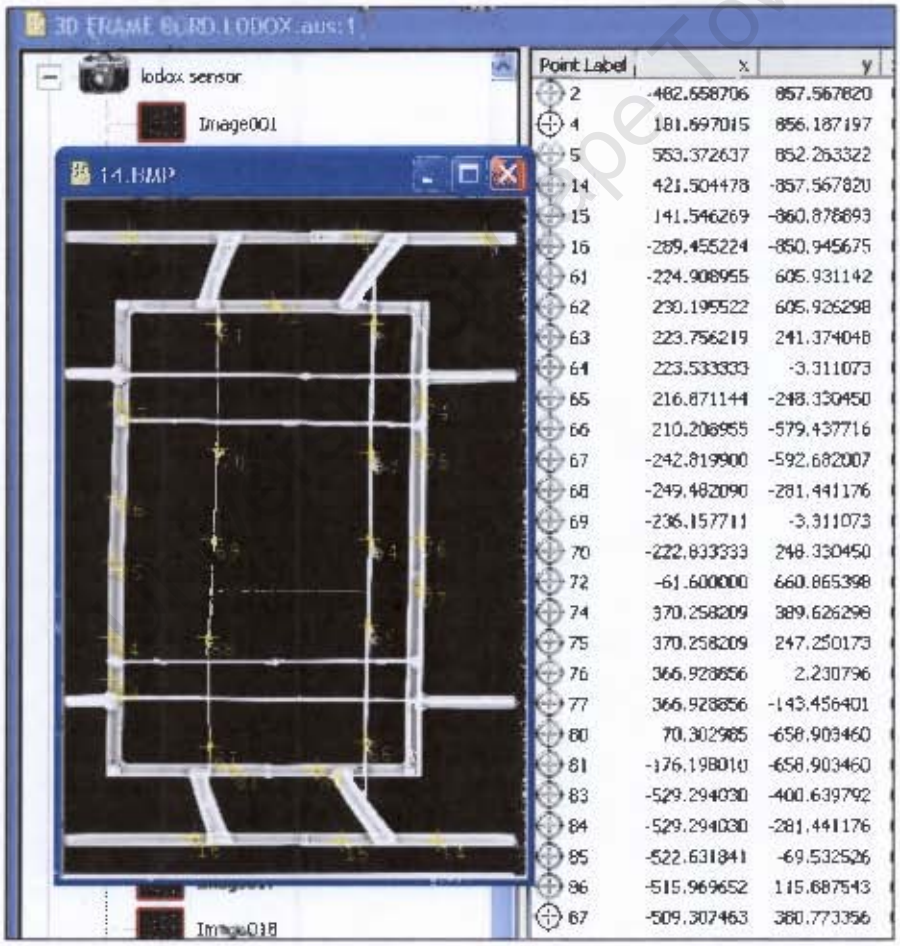

Figure 5-3 Measured target points of Statscan 14 degree image for the big metal frame

The point localization error (D) was computed by taking difference between phototogrammetry derived coordinates (X_P, Y_P, Z_P) and computed DLT coordinates (X_C, Y_C, Z_C). Thus the RMS (XYZ) was obtained as shown in equation 3-4. Table 5-2 represents the tabulated results for the reconstruction using thirteen different images with an increasing orientation angle from 0 degree machine setup.

Experimental Case	Big frame image DLT combinations (deg.)	Convergence Angle (deg.)	RMS(XYZ) (mm)
1	5 & 9	4	37.3
2	5 & 14	9	30.7
3	5 & 18	13	40.2
4	5 & 22	17	42.5
5	5 & 26	21	41.2
6	5 & 30	25	39.7
7	5 & 34	29	37.0
8	5 & 39	34	37.2
9	5 & 43	38	32.1
10	5 & 45	40	36.7
11	5 & 49	44	31.9
12	5 & 53	48	37.9

Table 5-2 Big frame reconstruction RMS (XYZ), (from 5^0 – 53^0 images).

The presented results showed gradual changes in 3D localization accuracy obtained using images scanned between 5 and 53 degrees orientation. The accuracy obtained ranged between 30 and 43 mm when reconstruction of the target points on the big frame was done. This accuracy is quite unacceptable for medical applications, especially as measurements of soft tissue, if at all possible, would be even less accurate than measurements to well defined targets. Measurements on soft tissue usually cannot be done accurately as the human body

generally does not provide distinct points where measurements can be done repeatedly.

Target points at the edge of the frame appeared to be more displaced as compared to those images at the center mid-position of the frame (see figure 5-4 and table 5-3). The changes were irregular and showed no significant trend. Further experiments were conducted using images of the small metal frame taken along the whole scan range of the Statscan C-arm. Figure 5-4 is a graphical representation of positioning accuracy for the big frame from two image DLT solutions.

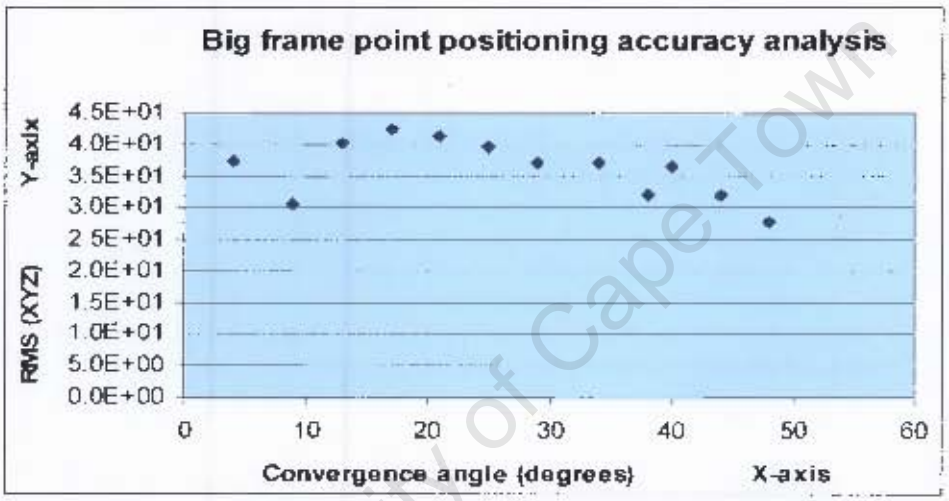

Figure 5-4 Plot of Statscan big frame image orientations against point positioning accuracy RMS (XYZ).

The results obtained from 5 degree and 53 degree image combination were used to plot the reconstructed points in 3D space. *Matlab* software was used to display the 3D graphic of the points. The points in red are the photogrammetry control points while the black points are the reconstructed points. Points within the inside of the metal frame were found to be reconstructed at a higher accuracy as compared to those at the edges of the frame. Such a disparity in the accuracy obtained was due to the divergence in the imaging X-ray beam. Points at the edge of the metal frame were imaged at the edge of the X-ray beam, while those

points within the inside of the frame were imaged at the central part of the X-ray beam with less divergence.

5.1.2.1 Effect of X-ray beam divergence on point positioning accuracy

The big frame occupied the whole scan space on the Statscan X-ray platform. The targets on the frame edges were imaged at the outward side of the X-ray beam which diverges from the centre. These edge points were 4, 5, 75, 76, 77, 78, 80, 83, 84, 85 and 86. The points in the middle of the frame (61, 62, 63, 64, 65, 66, 68, 69, 70), were imaged at the near parallel central X-ray beam. For all the experimental cases outlined in section 5.1.2, the positioning accuracy of the edge points and mid points was computed. Positioning accuracy of the edge points was lower than that of the mid points. The overall accuracy for all the points on the big frame was affected by the X-ray beam divergence. The results are shown in table 5-3 and represented graphically in figure 5-5.

Experiment Case	Image combination(deg.)	Convergence angle(deg.)	Edge points RMS(mm)	Mid points RMS(mm)
1	5 & 9	4	44.7	22.6
2	5 & 14	9	37.5	16.7
3	5 & 18	13	50.1	18.2
4	5 & 22	17	52.0	22.3
5	5 & 26	21	50.4	21.8
6	5 & 30	25	48.7	20.7
7	5 & 34	29	45.4	19.5
8	5 & 39	34	46.5	16.0
9	5 & 43	38	40.6	16.4
10	5 & 45	40	50.3	17.1
11	5 & 49	44	44.7	16.1
12	5 & 53	48	34.7	14.5

Table 5-3 Positioning accuracy for big frame edge and mid points.

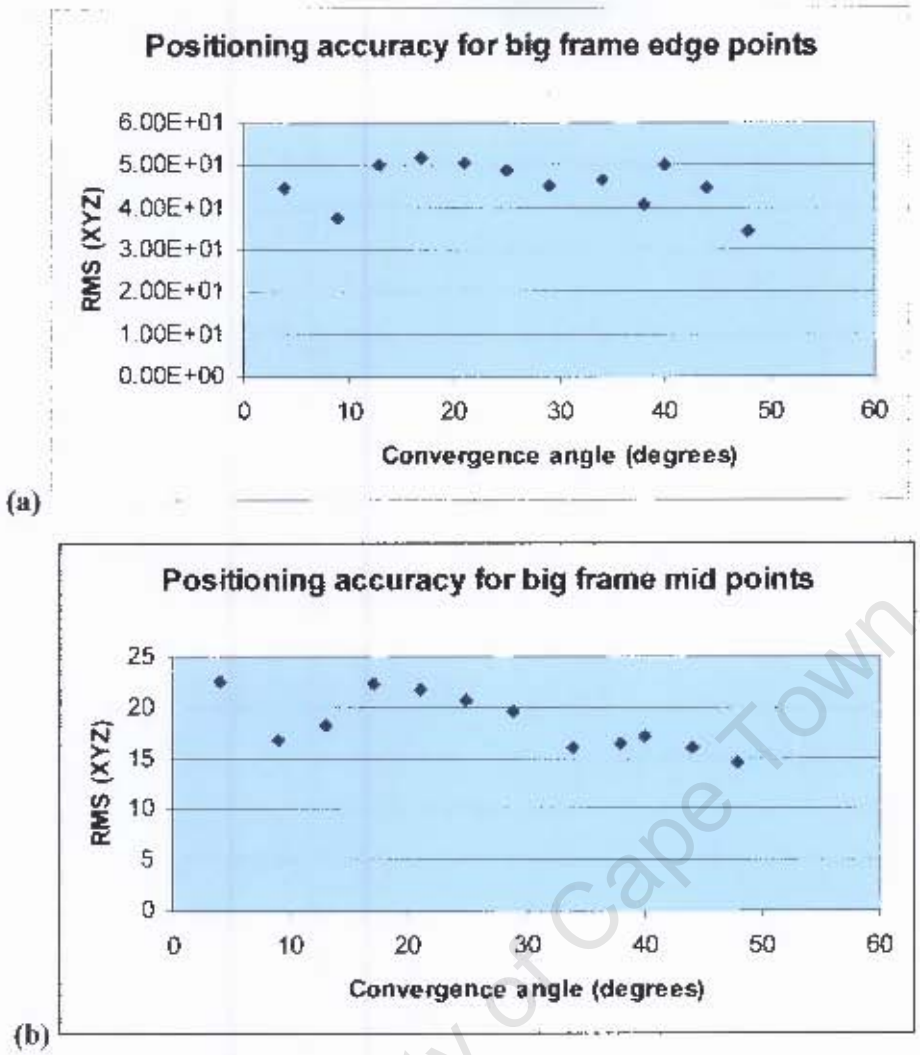

Figure 5-5 Big frame positioning accuracy for edge points (a) and mid points (b)

The results obtained from the big frame experiments showed that the Statscan system cannot be used to image a big object covering the whole X-ray platform. The poor accuracy obtained when the diverged X-ray beam was used to image the big frame would be repeated when imaging a human body on the same X-ray platform. Therefore, the method investigated would not be appropriate when full human body imaging and 3D localization has to be done on required areas of interest.

5.1.3 Reconstruction of the small frame

Image coordinates of all the target points on the small frame were measured from all the images recorded between 0 degrees and 45 degrees range in the Statscan C-arm rotation. Six control points were used in the DLT solution and were chosen from the corners. The minimum number of six was found to be sufficient after testing with a number of experimental cases. The 3D point reconstruction process was achieved through combining each successive image with the image taken at 0 degree position. This procedure was aimed at investigating the change in point localization accuracy with increase in convergence angle. The results showed that the coordinates of points lying on the surface of the X-ray table were closer to those of the control points than the ones at the top of the frame. The dimensions of the small metal frame are 350mm*310mm*265mm. Figure 5-6 shows labeled point targets on the small frame Statscan image scanned at 10 degrees orientation. The bones inside the frame provide orientation for the image.

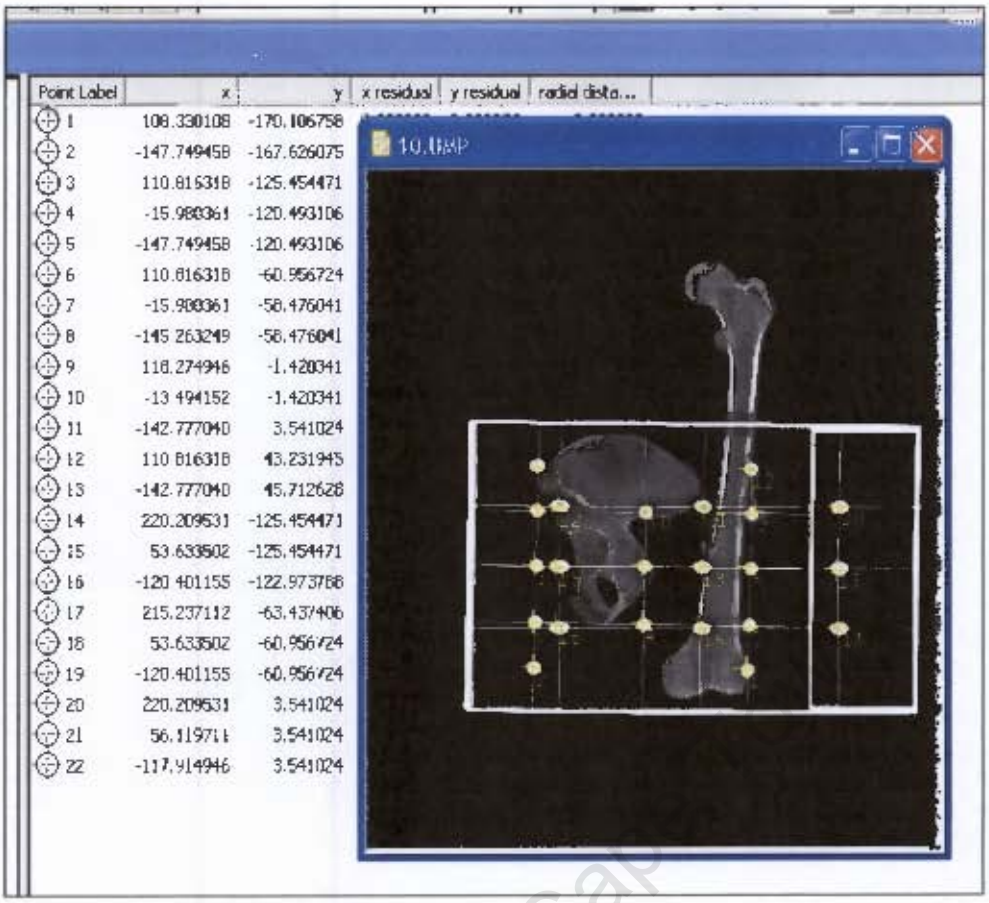

Figure 5-6 Labeled target points for Statscan small metal frame image taken at 10 degrees.

The reconstruction accuracy of the small metal frame was better than that of the big frame. The explanation for the difference in positioning accuracy of the two frames is due to their different sizes. The small frame was imaged at the central part of the X-ray beam with less divergence. This was unlike the case in the big frame because the whole beam was used to cover the frame which occupied the whole width of the scanning platform. Figure 5-7 shows all the point targets in 3D space together with the arrangement of chosen control points used in the DLT solution.

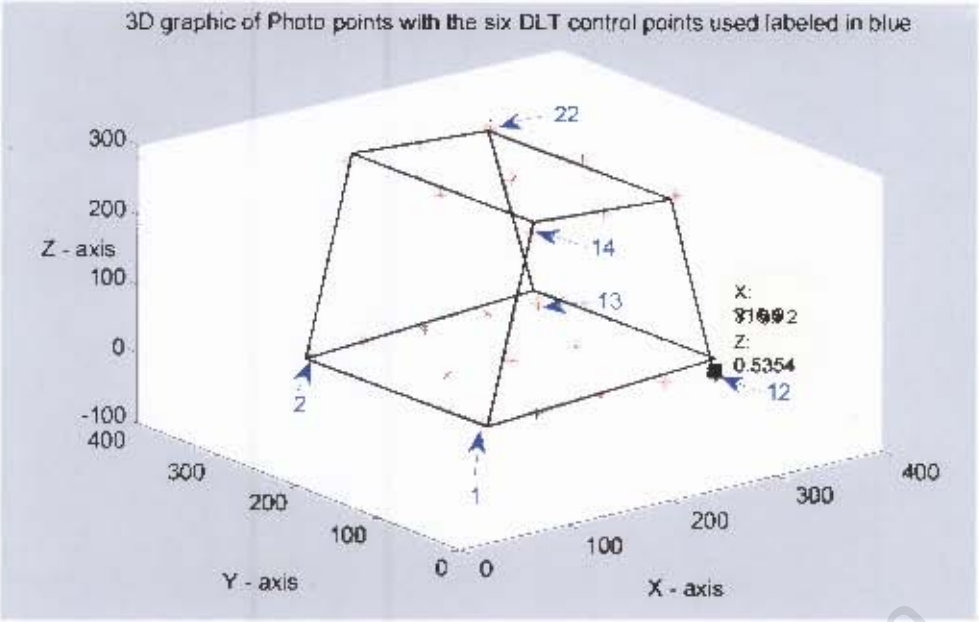

Figure 5-7 3D Display of the small frame control points used in DLT solution.

Figure 5-8(a) shows point labels for all the targets on the small metal frame. The point positions of reconstructed points using 0 & 45 degree image combination and the photogrammetric control coordinates has been shown by plotting the reconstructed points in black and the space control values in red. Point nine and twelve that are at the bottom of the frame, lying on the platform have been found to merge as one point due to high positioning accuracy as shown in the display in figure 5-8(b).

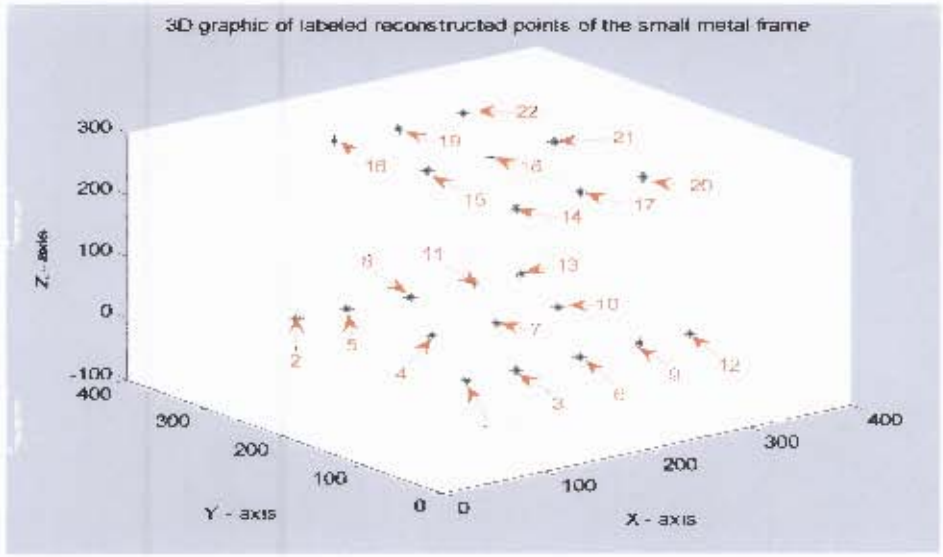

(a)

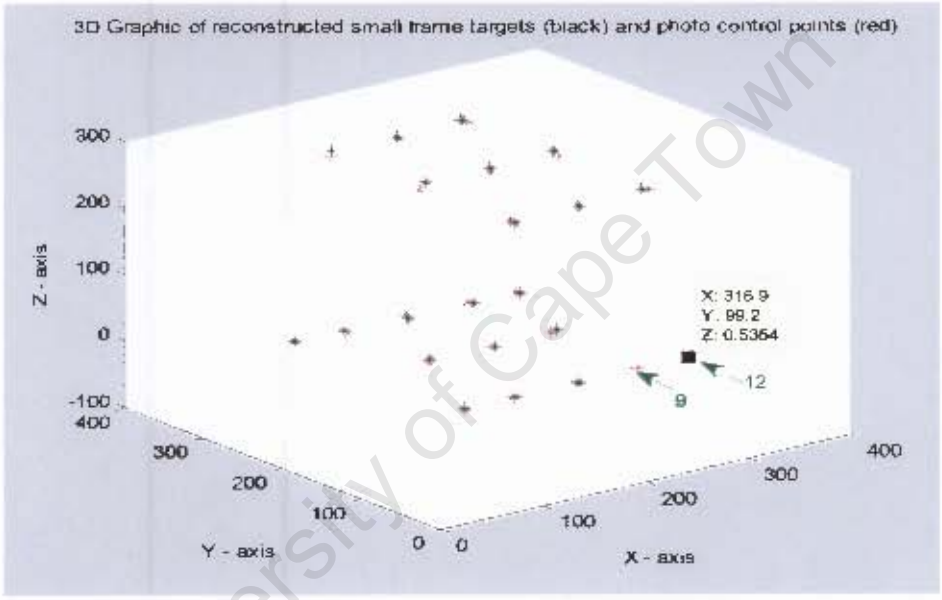

(b)

Figure 5-8 Labeled points of Statscan small frame reconstructed (a), and both control frame points (red) plotted together with respective reconstructed points (black) (b).

Table 5-4 shows the tabulation of computed RMS (XYZ) for all images used. The first image taken at 0 degrees was combined with the rest of the images in the DLT solution. This progressive increase of convergence angle resulted in an inverse proportionality between the intersection angle and computed RMS (XYZ). Figure 5-9 represents the relationship

between reconstruction accuracy with increase in convergence angle for the twenty two reconstructed target points.

Experimental Case	Small frame Image Combination (deg.)	Convergence Angle (deg.)	RMS(XYZ) (mm)
1	00&05	5	7.5
2	00&09	9	7.1
3	00&14	14	6.2
4	00&18	18	6.8
5	00&22	22	5.8
6	00&26	26	5.3
7	00&30	30	5.5
8	00&34	34	4.6
9	00&39	39	4.2
10	00&43	43	3.5
11	00&45	45	3.1

Table 5-4 Point positioning accuracy for the Statscan small metal frame, achieved using two image combinations in DLT solution (0-45 degree images).

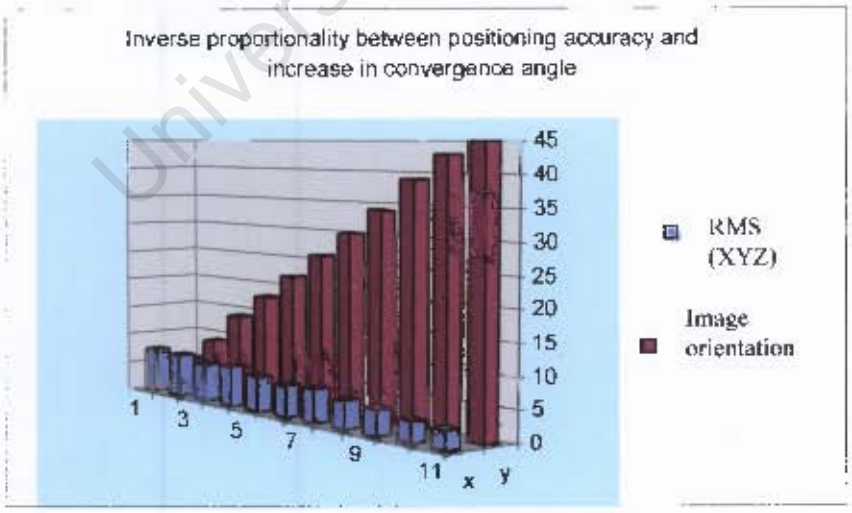

Figure 5-9 Reconstruction accuracy for Statscan small frame versus convergence angle (0 – 45 degrees images).

The points lying on the X-ray platform (1, 2, 3, 4, 5, 6, 7, 8, 9, 10, 11, 12 and 13) have been localized at 1.9mm root mean square error (RMS) in XYZ. Those points positioned above the X-ray platform, (14, 15, 16, 17, 18, 19, 20, 21, 22) have been localized at RMS (XYZ) of 4.3mm. The accuracy in positioning the top plane and bottom plane of the small frame for all the experiments with 0 to 45 degrees images are shown in table 5-5. Figure 5-10 (a) and (b) show the graphs for each case.

Experiment Case	Images Combinations (deg.)	Convergence angle (deg.)	Bottom Points RMS(XYZ) (mm)	Top points RMS(XYZ) (mm)	All points RMS (XYZ) (mm)
1	00 & 05	5	6.0	9.1	7.5
2	00 & 09	9	5.4	9.1	7.1
3	00 & 14	14	4.0	8.5	6.2
4	00 & 18	18	3.9	9.5	6.8
5	00 & 22	22	3.2	8.2	5.8
6	00 & 26	26	2.7	7.6	5.3
7	00 & 30	30	3.0	7.8	5.5
8	00 & 34	34	2.8	6.4	4.6
9	00 & 39	39	2.3	5.9	4.2
10	00 & 43	43	2.0	5.0	3.5
11	00 & 45	45	1.9	4.3	3.1

Table 5-5 Positioning accuracy for Statscan points on X-ray platform (bottom) points and above platform (top) points of small frame.

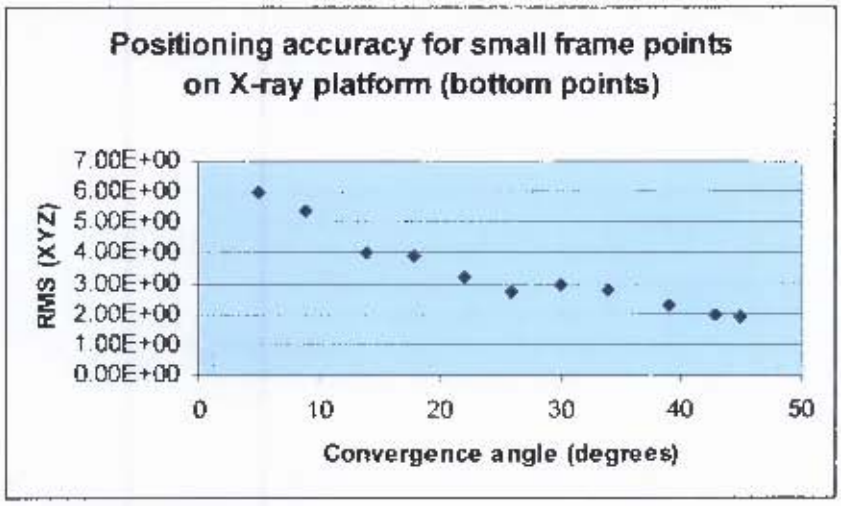

(a)

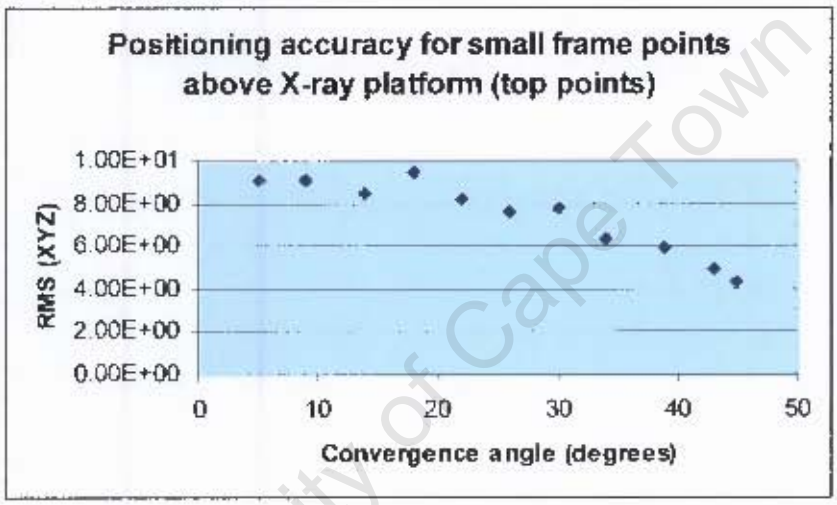

(b)

Figure 5-10 Positioning accuracy for small frame bottom (a) and top (b) points on the Statscan X-ray platform.

The accuracy obtained for the small frame experiments was significantly better than that achieved for the big frame. The small frame was imaged at the central part of the X-ray beam while the big frame was imaged at the more diverged edges of the X-ray beam. From these different experiments, it can be deduced that if object scanning can be restricted at the central part of the Statscan platform, high accuracy can be achieved in 3D point localization. However, this cannot be practical in most cases where the system is used to scan whole human body.

5.1.3.1 Comparison between reconstruction using two image, and more than two images at a time

Progressive addition of images in the DLT solution was done using the same images used in the two image solution. It was found that the reconstruction accuracy achieved using two images at a time improved with every image combination up to 45 degrees image orientation. However, the accuracy achieved using two images at a time was in most cases higher as compared to that attained with all the images combined together in the DLT solution. This is not typical for the modelling of photogrammetric observations where accuracy increases with an increase in the number of images used. The relatively high accuracy for small image numbers is likely to be the limited number of degrees of freedom which occur in this case. In such cases least squares modelling can result in exaggerated accuracies. The results for the experiments are given in table 5-6.

	Two image combinations in DLT solution		More than 2 images DLT combination	
Experimental Case	Convergence Angle(deg.)	RMS (XYZ) (mm)	No. of images	RMS (XYZ) (mm)
1	5	7.5	2	7.5
2	9	7.1	3	7.0
3	14	6.2	4	6.5
4	18	6.8	5	7.0
5	22	5.8	6	6.4
6	26	5.3	7	5.9
7	30	5.5	8	5.8
8	34	4.6	9	5.3
9	39	4.2	10	4.9
10	43	3.5	11	4.4
11	45	3.1	12	4.0

Table 5-6 Comparison between two Statscan images for the small frame and more than two images combined in DLT solution.

The tabulated data has been plotted to visualize the accuracy trends in both cases as shown in figure 5-11 (a) and (b).

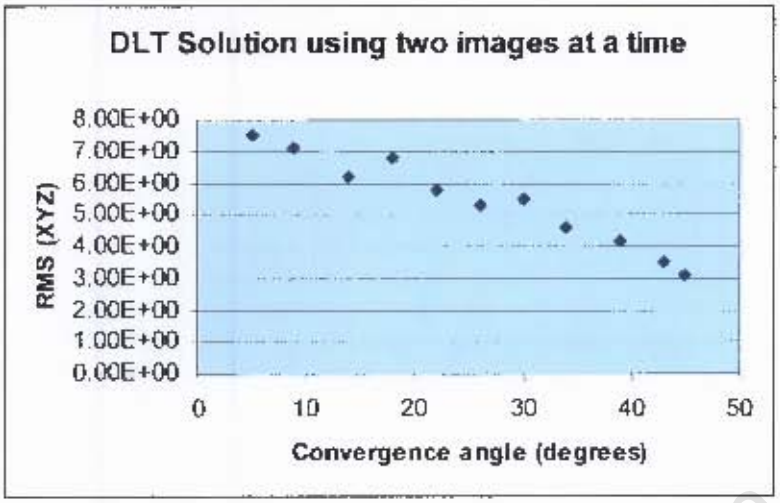

Figure 5-11(a) Convergence angle against positioning accuracy for the Statscan small frame (0-45 degrees images).

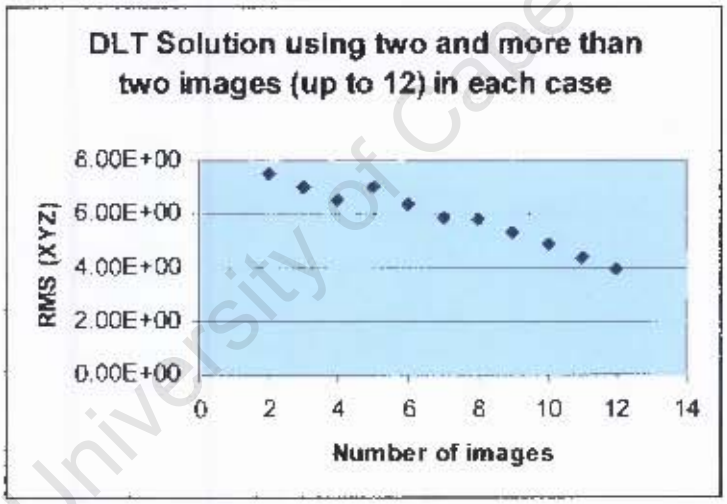

Figure 5-11(b) Number of images against positioning accuracy for the Statscan small frame (0 – 45 degrees images).

5.1.3.2 Optimal scan range for the Statscan system

Images of the small metal frame were recorded at an interval of near 5 degrees within the full machine range (0 – 90 degrees). The system performance seemed to fluctuate within close similar convergence angles as shown in images taken between 0 – 45 degrees, and when scans were repeated for 0 – 90 degrees range. The range between 45 degrees and 60 degrees showed the highest accuracy in point reconstruction. This range can be taken as the Statscan optimal scanning range acquiring images to be used in 3D reconstruction. Beyond 60 degrees, the accuracy decreases with irregular trend. Table 5-7 gives the positioning accuracies obtained. Figure 5-12 visualizes the positioning accuracy changes in each successive reconstruction. In order to show the trend, second order polynomial curve fitting has been done.

Experiment Case	Images (deg.)	Convergence angle (deg.)	RMS(XYZ) (mm)
1	0 & 4	4	19.4
2	0 &10	10	13.3
3	0 &15	15	10.9
4	0 & 20	20	8.1
5	0 & 24	24	8.9
6	0 & 30	30	7.2
7	0 & 34	34	7.3
8	0 & 40	40	5.6
9	0 & 45	45	4.4
10	0 & 50	50	5.0
11	0 & 55	55	4.7
12	0 & 60	60	4.4
13	0 & 65	65	6.9
14	0 & 69	69	7.6
15	0 & 74	74	9.9
16	0 & 84	84	3.9
17	0 & 90	90	7.2

Table 5-7 Point positioning accuracy for Statscan small frame with images taken between 0 and 90 degrees.

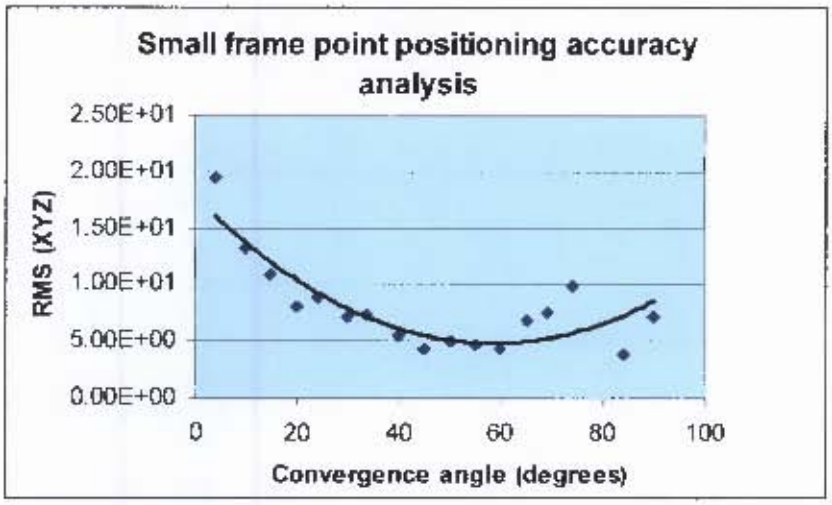

Figure 5-12 Positioning accuracy RMS (XYZ) against convergence angle for Statscan small frame (0 – 90 degree images).

From the trend shown in figure 5-12, accuracy was found to deteriorate beyond an optimal scan range. Increase in convergence angle increases the depth of the frame in object space, thus resulting in better accuracy within the optimal scan range.

CHAPTER SIX

6.0 DISCUSSION OF RESULTS, CONLUSION AND RECOMMENDATIONS

The thesis explored the suitability of the Direct Linear Transformation as a method for the determination of 3D coordinates of targeted points from multiple images acquired with the Statscan X-ray system. This investigation was carried out as a first step towards the development of a method to determine the accurate positions of points on or inside the human body. The major causes of errors in three-dimensional point localization using Statscan images were firstly, the X-ray beam divergence and secondly, the position of the point targets above the X-ray platform. These factors were demonstrated in figures 5-5 and 5-10 respectively.

The experiments carried out with two reference frames showed that point positions could be established with RMS values in the *mm* range in the middle axis of the X-ray patient platform. This range of acceptable *mm* accuracies extends about 15 to 20 cm sideways towards the edge of the table and to about 20 cm above the table surface. Beyond this range, accuracy deteriorated significantly reaching RMS values of 30 to 40 mm. The experiments further showed that the inclusion of control points close to the table edges and more than 20 cm above the table resulted in lower accuracies for the L - parameters of the DLT solution than those derived from points close to the center axis only. As the accuracy of the L - parameters propagates into accuracy of the final coordinates of newly determined points, it is essential to restrict the space of the control points to the above described limits.

If one adopts the usual approach of surrounding the object by known control points, then the limited space with an acceptable accuracy potential for the L - terms would not be large enough to enclose an adult human body surrounded by suitably positioned control points. This shortcoming can be overcome by making use of two further observations made in the course of this investigation. These observations were firstly, that the best image orientation angles are 0^0 and 40^0 to 60^0, and secondly, that no significant improvement could be achieved when using more than two images. The results in table 5-6 have shown that the combination of 5 degree and 45 degree images gave RMS (XYZ) value of 3.1mm while all the twelve images combined resulted in RMS (XYZ) value of 4.0 mm for the small frame. This observation contradicts the theory of adjustment and observations, and can be investigated in further research. The possible observation method deduced from this is as follows:

1. A frame with well distributed control points with accurate 3D coordinates and of approximately the size of a human body is placed on the X-ray table and imaged with the X-ray beam in the 0 degree position. This makes it possible to determine L parameters for this ray orientation.

2. The frame is removed; the patient is positioned in the control space; and an X-ray image of the patient is taken.

3. The X-ray source is rotated to a new position between 40^0 and 60^0 and a second image of the patient is acquired.

4. The patient is removed and replaced by the frame. A final image of the frame is now acquired.

Steps 1 and 4 serve to determine the L-parameters for the two X-ray source positions, while steps 2 and 3 provide the image coordinates of

the required object points on or inside the patient's body. This approach can only then result in accurate point positions, if the patient remains motionless for the duration of steps 2 and 3. An alternative to this observation design would be simultaneous imaging from two X-ray sources, one with 0^0 orientations and the other with an orientation between 40^0 and 60^0.

A further restriction in the use of the scanner as a 3D positioning device results from the need for well defined point. This means that positions on soft tissues cannot be determined unless the required points are clearly defined in the scan images. Positions and dimensions of bones and foreign objects inside the human body are easier to establish.

Abdel-Aziz, Y.A., Karara, H.M., (1971); Direct linear transformation from comparator coordinates into object space coordinates in close-range photogrammetry, *Proceedings of the ASP symposium on Close-Range Photogrammetry, pp 420-475.*

Adams, L.P., (1981); X-ray Stereo-photogrammetry locating the precise, three-dimensional position of image points. *Medical and Biological Engineering and Computing, Vol. 19, pp 569 – 578.*

Atkinson, K.B., (1996); Close Range Photogrammetry and Machine Vision.

Brown, D., (1989); A strategy for multi - camera On-the-job self calibration. *Institut Fur Photogrammetrie Stuttgart.* www.vision.caltech.edu *(accessed July, 2005).*

Douglas, T.S. et al., (2004); Three-dimensional point localization in low-dose X-ray images using Stereo-photogrammetry. *Medical & Biological Engineering & Computing, Vol. 42, pp 37-43.*

Faig, W., (1976); Photogrammetric Potentials of Non-Metric cameras – Report of ISP Working Group V/2 18th ISP Congress, Helsinki. *Photogrammetric Engineering and Remote Sensing, pp 47 – 49.*

El-Manadili, Y. and Novak, K., (1996); Precision rectification of SPOT imagery using the Direct Linear Transformation model, *Photogrammetric Engineering and Remote Sensing, Vol. 62, pp 67-72.*

Faig, W. and Shih, T.Y., (1986); Critical Configuration of Object Space Control Points for the Direct Linear Transformation, *Proceedings of the Symposium Real-Time Photogrammetry- A new challenge, ISPRS, Vol. 26, part 5, pp 23-29.*

Fraser, C.S. and Edmundson, K.L., (2000); Design and Implementation of a Computational Processing System for Off-Line Digital Close-Range Photogrammetry, *ISPRS Journal of Photogrammetry & Remote Sensing,* 55(2): pp94-104.

Fraser, C.S., (2001); *Australis* User Manual, (*University of Melbourne*).

Fritsch, D. and Stallmann, D., (200); Rigorous Photogrammetric Processing of high resolution Satellite Imagery, *ISPRS, Vol. XXXIII, Armsterdam.*

Fryer, J.C., (1986); Lens Distortion for Close Range Photogrammetry, *Proceedings of the Symposium Real-Time Photogrammetry· A new challenge, ISPRS, Vol. 26, part 5, pp30 37.*

Fryer, J.C., (1989); Camera Calibration in Non-Topographic Photogrammetry pp 59 – 69.

Gonzales, R.C. and Woods, R.E., (2002); Digital Image Processing – International Edition (2nd Edition).

Gonzales, R.C., Woods, R.E. and Eddins, S.L., (2004); Digital Image Processing using *Matlab*.

Grossmann, W., (1975); *Vermessungskunde II. Sammlung Göschen de Gruyter.*

Hicks, C.R., Turner, K.V. (Jr.), (1999); Fundamental Concepts in the Design of Experiments (5th Edition).

Imaginis Corporation website, (1997-2006); History of Medical Diagnosis and Diagnostic Imaging, http://imaginis.com/faq/history.asp?mode=1 (updated: Feb 8, 2000), *(retrieved March 13, 2006).*

Internet sources;
http://www.inventors.about.com/library/inventors/blxray.htm

http://www.ablesw.com/3d-doctor/surgmod.html

http://www.neurosciencecenter.com/NCoW/x-ray.html

http://www.nuclear.kth.se

ISPRS, (1986, June 16-19); Proceedings of the Symposium held in Ottawa, Canada. Real-Time Photogrammetry – A new challenge.

Karara, H.M. (1989); Non-Topographic Photogrammetry (2nd Edition)

Kasser, M. and Egels, Y., (2002); Digital Photogrammetry.

South African Innovations, (2005, August 11); About South Africa, Science & Technology, *Lifesaving SA innovation.* http://www.southafrica.info/ess_info/sa_glance/scitech/statscan.htm *(retrieved April 19, 2006).*

Lodox website; http://www.lodox.com/

Marder, M., (2005, March); Comparison of Calibration Algorithms for a Low-Resolution, Wide Angle, 3D Camera. *Master of Science Thesis, Stockholm, Sweden, IR – SB – EX – 0511.*

Marzan, G.T. and Karara, H.M., (1976, January); "Rational Design for Close Range Photogrammetry"; *A report on a study sponsored by the National Science Foundation – as a part of research Grant GK-11655*; Civil Engineering Studies-Photogrammetry Series No. 43; University of Illinois at Urbana-Chamaign (Urbana, Illinois 61801), pp 156-185.

Mikhail, E.M., Bethel, J.S. and McGlone, J.C., (2001); Introduction to Modern Photogrammetry.

Montgomery, D.C., (1976, 1984); Design and Analysis of Experiments (2nd Edition).

Parsaye, K. and Chignell, M., (1993); Intelligent Database tools and Applications - *Hyperinformation Access, Data Quality, Visualization and Automatic Discovery.*

Pennsylvania State University web site (1993); A Century of Radiology; A project of Radiology Centennial, Inc
http://www.x-ray.hmc.psu.edu/rci/centennial.html/
(accessed March 18, 2006)

Rüther, H., (2005, APG313S); Numerical Methods in Geomatics lecture notes (*unpublished*).

Savopol, F. and Armenakis, C., (1998); Modelling of the IRS-IC Satellite Pan stereo imagery using DLT approach, *International Archives of Photogrammetry and Remote Sensing, Vol. 32, part 4, pp511-514, Stuttgurt, Germany.*

Scheelke, M., Potgieter, H. and Mattieu de Villiers, (2005, February) *(paper);* "System characterization of the STATSCAN full body slit scanning radiography machine: Theory and experiment." *Proceedings of SPIE Medical Imaging, San Diego.*

Tiggelen, R., JBR-BTR, (2002) 85: pp266-270; Historical Article, *In search for the Third Dimension: From Radio stereoscopy to three-dimensional Imaging,*
http://www.radiology-museum.be/pdf/article_0081.pdf
(accessed March 18, 2006)

Van Geems, (1995) – A two-dimensional projective transformation approach to solve for 3D Coordinates from CT surviews, PhD. Dissertation, pp 44-47 and pp 192-194.

Veress, et al., (1979); Analytical Approach to X-ray Photogrammetry. Photogrammetric Engineering and Remote Sensing, 43 (12):1503-1510.

Veress, S.A. and Karara, H.M., (1989); X-ray Photogrammetry, System, and Applications (pp 167-186 of Non – Topographic Photogrammetry).

Williams, H.P., (2003); Model Building in Mathematical Programming (4th Edition).

Wolf, P.R. and Dewitt, B.A., (1974, 1983, 2000); Elements of Photogrammetry *with Applications in GIS* (3RD Edition).

Wolf, P.R. and Ghilani, C.D., (1997); Adjustment Computations, *Statistics and Least Squares in Surveying and GIS.*